JOURNAL OF GEOPHYSICAL RESEARCH, VOL. 114, D09307, doi:10.1029/2008JD011186, 2009

Click Here for Full Article

Formation of ozone and growth of aerosols in young smoke plumes from biomass burning: 2. Three-dimensional Eulerian studies

Matthew James Alvarado,[1,2] Chien Wang,[1] and Ronald G. Prinn[1]

Received 23 September 2008; revised 10 February 2009; accepted 24 February 2009; published 9 May 2009.

[1] Global-scale models of atmospheric chemistry (GACMs) "mix" biomass burning emissions into grid boxes with horizontal scales of 10–200 km. This ignores the complex nonlinear transformations that take place in the young smoke plumes. Here we use a new gas- and aerosol-phase chemistry model called Aerosol Simulation Program (ASP) and a 3-D Eulerian smoke plume model to simulate the fluid dynamics, radiative transfer, gas-phase chemistry, and aerosol-phase chemistry of the Timbavati smoke plume observed during SAFARI 2000. We then compare the results of the 3-D plume model with those of an Eulerian box model, which is used as an analog for the large grid boxes of GACMs. The 3-D plume model matched the observed plume injection height but required a large minimum horizontal diffusion coefficient to match the observed horizontal dispersion of the plume. Absorption and scattering by smoke aerosols reduced the modeled photolysis rates in the plume by 10–20%. Increasing the heterogeneous production of HONO and H_2SO_4 in the model and including uncharacterized organic species using monoterpenes as a proxy compound improves the model-observation match. Direct measurements of OH in the smoke plumes would be an excellent way to determine if heterogeneous production of HONO is taking place. The automatic dilution of smoke plume emissions into the large grid boxes of global models can result in large errors in predicted concentrations of O_3, NO_x and aerosol species downwind. We discuss several potential approaches that could reduce these errors.

Citation: Alvarado, M. J., C. Wang, and R. G. Prinn (2009), Formation of ozone and growth of aerosols in young smoke plumes from biomass burning: 2. Three-dimensional Eulerian studies, *J. Geophys. Res.*, *114*, D09307, doi:10.1029/2008JD011186.

1. Introduction

[2] The combustion of biomass is a major source of atmospheric trace gases and aerosols which can impact global atmospheric chemistry and climate [*Crutzen and Andreae*, 1990; *Intergovernmental Panel on Climate Change*, 2001]. In general, regional- and global-scale models of atmospheric chemistry and climate take estimates for the primary emissions of trace gases and aerosols from biomass burning and "mix" them automatically into much larger-scale grid boxes (e.g., with 10–200 km horizontal scales) before performing any calculations of gas-phase chemistry, aerosol-phase chemistry, or aerosol dynamics. This procedure ignores the substantial nonlinear chemical and physical transformations (e.g., gas-phase chemistry, coagulation of aerosols, condensation of vapors, etc.) that can take place in the highly concentrated environment of young biomass burning smoke plumes [*Andreae and Merlet*, 2001; *Jost et al.*, 2003]. These transformations can lead to significant changes in the gas phase composition of the smoke and the number, size, composition, and shape of the emitted particles [*Jost et al.*, 2003; *Hobbs et al.*, 2003; *Li et al.*, 2003; *Liousse et al.*, 1995; *Posfai et al.*, 2003; *Reid et al.*, 2005a, 2005b]. As these changes are not correctly included in large-scale models, these large-scale models may misrepresent the true impacts of biomass burning smoke on atmospheric chemistry and climate [*Jost et al.*, 2003].

[3] The goals of this paper and a companion paper [*Alvarado and Prinn*, 2009] are to model the growth of smoke particles within young biomass burning plumes, evaluate the impact of these particles on the gas-phase chemistry and formation of ozone within the plume, and estimate the errors caused by the aforementioned automatic dilution of plume emissions in global atmospheric chemistry models (GACMs). *Alvarado and Prinn* [2009] used a new gas- and aerosol-phase chemistry model (Aerosol Simulation Program (ASP)) to study the chemical evolution of three young smoke plumes from biomass burning in a Lagrangian framework. In this paper, we describe our 3-D Eulerian simulations of the fluid dynamics, radiative transfer, gas-phase chemistry, and aerosol-phase chemistry within

[1]Department of Earth, Atmospheric and Planetary Sciences, Massachusetts Institute of Technology, Cambridge, Massachusetts, USA.
[2]Now at School of Engineering and Applied Science, Harvard University, Cambridge, Massachusetts, USA.

Copyright 2009 by the American Geophysical Union.
0148-0227/09/2008JD011186$09.00

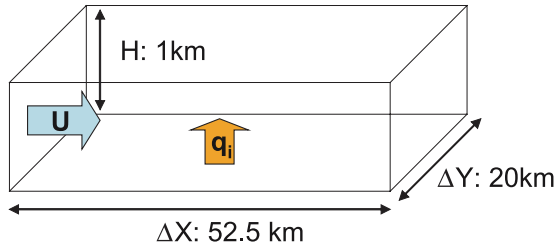

Figure 1. Schematic of the Eulerian box model. U is the horizontal wind speed, while q_i is the emissions flux of species i.

the smoke plume of the Timbavati South African savannah fire. To our knowledge, this is the first time all of these processes have been simulated simultaneously for a young biomass burning smoke plume. The 3-D Eulerian simulation allows us to evaluate the impact of plume buoyancy and dynamics on the formation of ozone and growth of aerosols within the smoke plume, to evaluate the impact of the aerosol particles on the actinic flux and photolysis rates within the smoke plume, to determine how the observed gas and aerosol concentrations might change because of different sampling heights during plume transects, and to make suggestions for future measurement campaigns.

[4] In addition, we estimate the errors caused by the automatic dilution approach of GACMs by comparing the results of our 3-D Eulerian simulation of the Timbavati smoke plume to the results of a single-box Eulerian model with the same horizontal scale (52.5 km × 20 km) as the full domain of our 3-D simulation. This Eulerian box model is used as an analog of the large-scale grid boxes of GACMs.

2. Model Description

2.1. Description of the 3-D Eulerian Plume Model

[5] To simulate the fluid dynamics of the smoke plume, we use an updated version of the Cloud Resolving Model (CRM6) of *Wang and Chang* [1993a]. CRM6 has been used in simulating the impact of deep convection on tropospheric chemistry and the interaction of aerosols, convection, and chemistry in clouds [*Wang and Chang*, 1993b; *Wang and Prinn*, 2000; *Wang*, 2005a, 2005b; *Ekman et al.*, 2006, 2007]. The modeled chemical and aerosol fields have been found to be in good agreement with observations in several case studies [*Wang and Prinn*, 2000; *Ekman et al.*, 2006; *Barth et al.*, 2007]. CRM6 was modified for this work to include a source of sensible heat, trace gases, and particles at the surface to simulate the heating and the various emissions from the fire. The equations of CRM6 are presented in Appendix A.

[6] The gas and aerosol chemistry for the Eulerian simulations is calculated using the Aerosol Simulation Program (ASP) described in detail by *Alvarado* [2008]. The ASP model integrates the gas-phase chemistry, gas-to-aerosol mass transfer, aerosol thermodynamics, and aerosol coagulation to calculate gas and aerosol concentrations, as well as aerosol optical properties.

2.2. Eulerian Box Model Description

[7] In order to evaluate the errors in the effective flux of gas and aerosol species to the global environment caused by the automatic dilution of biomass burning emissions into large-scale global model grid boxes, as is done in many GACMs, we created an Eulerian box model to use as an analog of a GACM grid box. We assume that both models will have the same gas and aerosol-phase chemical routines. The model is shown schematically in Figure 1. The model equations are presented in Appendix B.

[8] The chemical routines for the Eulerian box model and the 3-D Eulerian plume model are the same, allowing us to determine the errors caused by the automatic dilution of biomass burning emissions in large-scale grid boxes. However, there are other potentially important differences between the Eulerian box and 3-D plume models besides their differences in vertical and horizontal resolution. For example, the Eulerian box model calculates photolysis rates using TUV v.4.1 rather than the CRM6 routines, ignores the effect of aerosol particles on actinic flux and photolysis rates, and has no vertical mixing of compounds into or out of the box. Thus the box model is expected to have higher photolysis rates than the 3-D Eulerian model as discussed in section 4.1. The impact of vertical diffusion of compounds on the comparison between the two models is evaluated below by comparing concentrations of different tracer species in the models.

3. Three-Dimensional Eulerian Investigation of the Timbavati Plume

[9] Figure 2 shows the Eulerian domain and resolution used for the simulations of the Timbavati smoke plume. The total model domain size was 52.5 km × 20 km × 4 km with a resolution of 500 m × 1 km × 100 m. The width of the rectangular fire source was set at 2 km on the basis of observations [*Hobbs et al.*, 2003], with a downwind thickness of 500 m. The model was allowed to "spin up" for 10 min before the fire source was turned on, after which the model was run for 60 min. In the rest of this section we discuss the initial meteorological (section 3.1.1) and chemical (section 3.1.2) model state for the Timbavati plume simulation, describe the fire emissions of heat, trace gases, and particles (section 3.1.3), and describe the two chemistry cases used in our study (section 3.1.4).

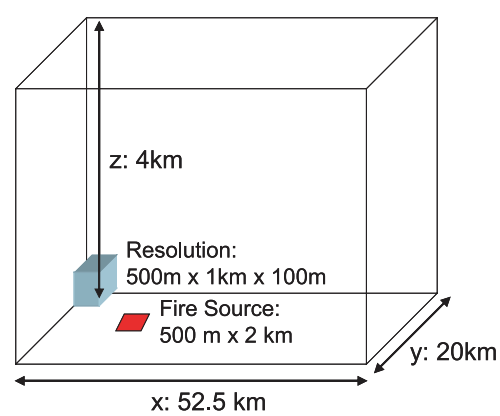

Figure 2. Domain size and resolution for the 3-D Eulerian simulations of the Timbavati smoke plume.

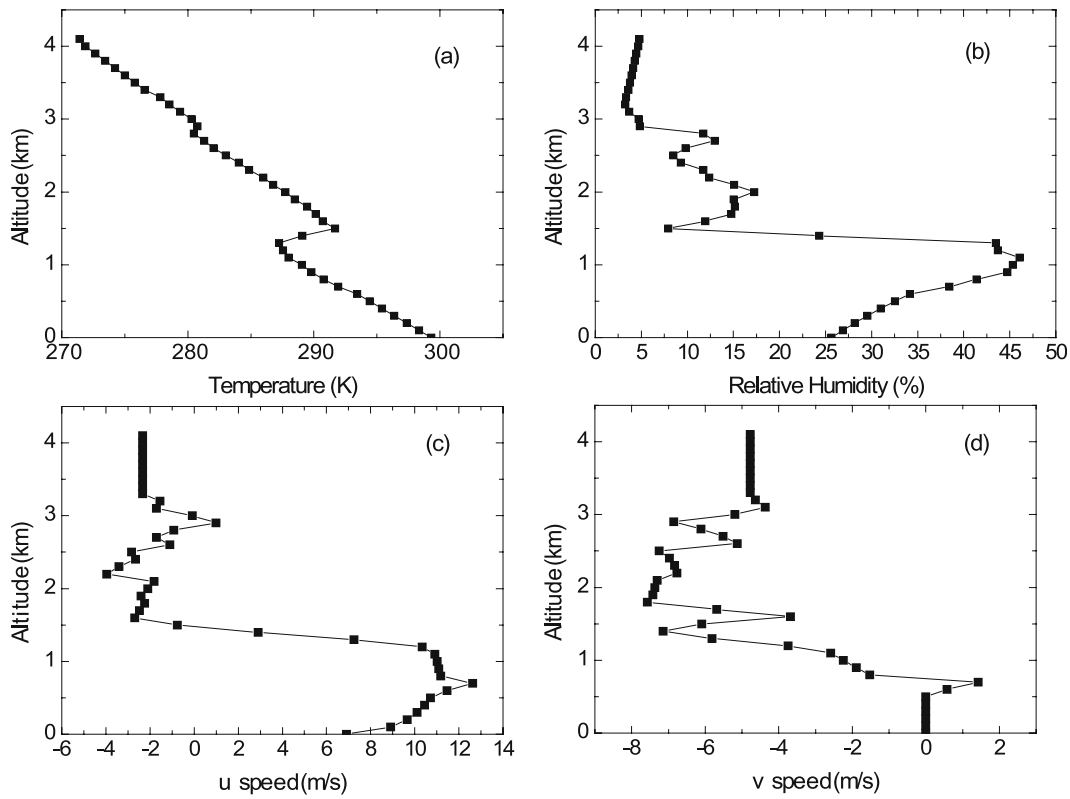

Figure 3. Initial profiles of (a) temperature, (b) relative humidity, and wind speed along the model (c) x axis and (d) y axis used in the 3-D Eulerian simulations of the Timbavati smoke plume. Data between 600 m and 3300 m are from *Hobbs et al.* [2003] and have been binned and averaged for every 100 m. The rest of the profile is extrapolated from the available data as described in the text.

3.1. Model Initialization

3.1.1. Meteorology

[10] The profiles for temperature, relative humidity, and horizontal winds used to initialize the Timbavati model simulations are shown in Figure 3. These are based on the vertical profiles measured between 600 m and 3300 m in altitude by *Hobbs et al.* [2003] upwind of the Timbavati fire between 0829 and 0840 UTC. The data were binned and averaged for every 100 m in altitude. The direction of the x axis and u wind was set to 160°, the measured wind direction at 600 m in altitude, with the y axis and v wind direction set perpendicular to this. For altitudes below 600 m, temperature was calculated assuming a dry adiabatic lapse rate and q_v (kg H_2O/kg moist air) was assumed to be constant. The wind direction below 600 m was held constant at 160° (thus, $v = 0$ below 600 m) while the wind speed (u) was assumed to follow a logarithmic profile with altitude. Above 3300 m, wind direction and speed were held constant, as was q_v. Temperature was calculated assuming that the observed lapse rate below 3300 m stayed constant with height to 4000 m. The data show a strong temperature inversion between 1.3 and 1.5 km in altitude, with corresponding rapid changes in other variables.

3.1.2. Gas and Aerosol Concentrations

[11] *Hobbs et al.* [2003] also measured the background vertical profiles of O_3 and SO_2 upwind of the Timbavati fire. These data were binned every 100 m and averaged to provide initial vertical profiles of O_3 and SO_2 for the Eulerian model simulations. The profiles are shown in Figure 4. The mole fractions are assumed to be constant below 600 m and above 3300 m in altitude.

[12] All other gas-phase species were assumed to have a constant mole fraction versus altitude, with the mole fraction chosen to match the background concentrations for Timbavati given by *Trentmann et al.* [2005]. To prevent numerical problems, all compounds with a background concentration of 0 were assumed to be present at a constant initial mole fraction of 1 ppt.

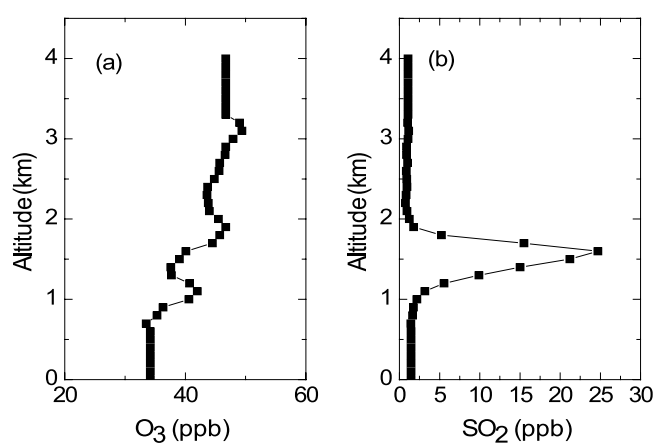

Figure 4. Initial mole fractions of (a) O_3 and (b) SO_2 versus height for the Timbavati smoke plume.

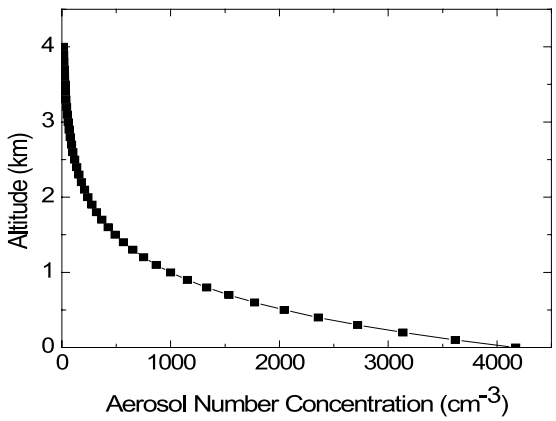

Figure 5. Initial aerosol number concentration versus height for the Timbavati smoke plume.

[13] The initial vertical profile of aerosol in the model was calculated assuming an exponential decay of aerosol concentration with height [*Seinfeld and Pandis*, 1998]. The aerosol number and mass concentrations at 1 km altitude were set to the values given for the background aerosol for Timbavati by *Alvarado and Prinn* [2009]. The initial aerosol number concentration versus height data for the Timbavati simulations is shown in Figure 5. The aerosol was simulated using a 4 bin size distribution, with 2 of the bins between 0.015 μm and 1 μm in radius. This is the smallest number of bins that could be used and still have the aerosol size distribution represent the optical properties of the 12 bin size distribution used in the Lagrangian experiments in the work by *Alvarado and Prinn* [2009].

3.1.3. Fire Emissions

[14] According to *Hobbs et al.* [2003], the Timbavati fire was ignited at 0801 UTC and burned for 3 h, burning 3.8×10^6 kg of biomass.

[15] In our model simulations, we assume the fire front moved in the downwind direction at a constant speed of 0.5 m/s. Using a value of 18,700 kJ/kg for the heat of combustion of biomass [*Trentmann et al.*, 2006] gives a total heat release of 6.6×10^9 W. Following *Trentmann et al.* [2002], we assume that 55% of the total heat released by the fire contributes to the buoyancy of the smoke plume while the rest is lost through longwave radiation, giving a buoyant heat release of 3.6×10^9 W.

[16] To calculate the emission of CO from the Timbavati fire, we used the USDA Fire Service Fire Emission Production Simulator (FEPS) v.1.1.0 (available at http://www.fs.fed.us/pnw/fera/feps/index.shtml). For the reported conditions of the Timbavati fire, FEPS estimated a CO release rate of 49.5 kg CO/s. The emission rate of water vapor was calculated using an emission factor of 0.5 kg H_2O/kg dry fuel [*Freitas et al.*, 2007]. The emissions of all other smoke gases were calculated using the emission ratios of these compounds to CO as reported by *Hobbs et al.* [2003] and *Trentmann et al.* [2005]. The emission ratios for aerosol species were calculated from the rescaled initial concentrations from the Lagrangian studies in the work by *Alvarado and Prinn* [2009] to better match the observed potassium concentrations.

3.1.4. Reference and Expanded Chemistry Cases

[17] The results of the Lagrangian modeling for the Timbavati plume from *Alvarado and Prinn* [2009] showed that the reference model simulation did not provide a good match with the observed formation of O_3 and growth of aerosols in the Timbavati smoke plume. We found that modeling the uncharacterized organic species in the smoke as a reactive monoterpene species (BIOH) and adding heterogeneous reactions of NO_2 and SO_2 significantly improved the match between the model and observations.

[18] On the basis of these results, we performed two simulations of the Timbavati smoke plume using the 3-D Eulerian plume model described above. In the first (hereafter the "reference chemistry" case), we assumed that the uncharacterized organic species were unreactive, and did not include any heterogeneous reactions of NO_2 or SO_2. In the second (hereafter the "expanded chemistry" case), we modeled the chemistry of the uncharacterized organic species using monoterpenes (BIOH) as a proxy for high-carbon-number reactive organic species that form organic aerosol. We also included the heterogeneous reactions $NO_2 \rightarrow 0.5\ HONO + 0.5\ HNO_3$ and $SO_2 \rightarrow H_2SO_4$ with uptake coefficients of 10^{-3} and 2×10^{-4}, respectively. *Alvarado and Prinn* [2009] and *Alvarado* [2008] contain further discussion of the model chemistry and the two chemical cases studied here. The results of both simulations are presented below.

3.2. Model Results and Comparison to Observations

[19] In this section we present the 3-D Eulerian model results for fluid dynamics and CO concentrations (section 3.2.1), O_3, OH, and NO_x concentrations (section 3.2.2), aerosol number and mass concentrations (sections 3.2.3 and 3.2.4, respectively), aerosol optical properties (section 3.2.5), and solar radiation and photolysis rates (section 3.2.6). All of the results shown in this section are provided at 60 min after the ignition of the fire source.

3.2.1. Fluid Dynamics and CO Concentrations

[20] Since the lifetime of CO (1–3 months) is very long compared to the 1 h time scale simulated here, we can assume it is an inert tracer and use the modeled concentration field for CO to evaluate how well the model simulates the injection height and horizontal dispersion of the Timbavati smoke plume. Figure 6 shows the modeled CO concentrations along the centerline of the plume (y = 0) and at 800 m in altitude. The CO mole fractions below 200 ppb represent the background environmental air outside of the plume, while values above 200 ppb represent the smoke plume. Figures 6a and 6b show the modeled CO concentrations when the minimum horizontal diffusion coefficient for chemical tracers (K_{min}) is set at 45 m^2/s (i.e., anytime the model-calculated horizontal diffusion coefficient is below K_{min}, it is set equal to K_{min}.) The modeled plume injection height of 0.6–1.0 km is fairly close to the observed injection height of the Timbavati smoke plume: specifically *Hobbs et al.* [2003] reported that most of the smoke was found between 0.5 and 0.9 km in altitude, with some puffs as high as 1.4–1.7 km. This injection height seems to be primarily determined by the strong initial temperature inversion between 1.3 and 1.5 km in altitude for the Timbavati smoke plume (Figure 3a). However, the modeled

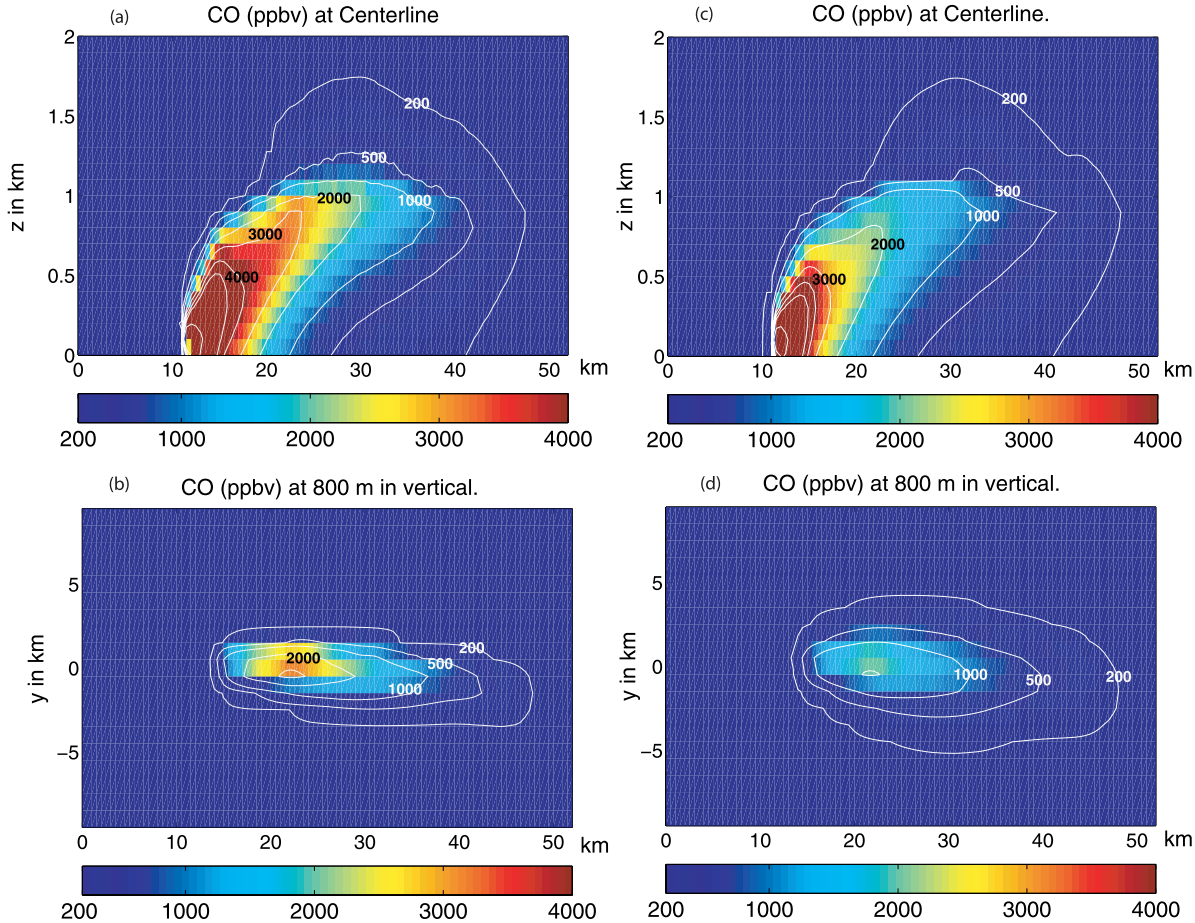

Figure 6. CO mole fractions for the Timbavati smoke plume along the plume centerline (y = 0 km) and at 800 m in altitude. (a and b) The low horizontal diffusion case (K_{min} = 45 m^2/s) and (c and d) the high horizontal diffusion case (K_{min} = 450 m^2/s).

horizontal plume width of 6 km is well below the 10–15 km width (at 26.2 km downwind) reported by *Hobbs et al.* [2003].

[21] There are two potential explanations for the underestimate of the horizontal dispersion of the Timbavati smoke plume. First, the first-order turbulent closure used in the model may be underestimating the subgrid-scale turbulent mixing of the plume. The effect of subgrid-scale turbulent mixing can be seen by observing the effect of increasing K_{min}. Figures 6c and 6d show the results of increasing K_{min} to 450 m^2/s. In this case, the horizontal plume width is approximately 10 km, providing a closer match to the observed value of 10–15 km. For this reason, we set K_{min} to 450 m^2/s for all the simulations discussed below.

[22] The second potential explanation is that the model is missing the effects of large-scale variability of the horizontal winds on the horizontal dispersion of the plume. In the model, the boundary conditions for the horizontal winds are held constant. However, the actual boundary layer winds may fluctuate with time on the scale of the smoke plume, increasing the horizontal spread of the smoke emissions. For example, the horizontal velocity spectra for a typical mixed boundary layer show a peak near a wavelength slightly larger than the height of the mixed layer, which for Timbavati is 1.3–1.5 km [*Kaimal et al.*, 1972; *Stull*, 1988]. These order 1.3–1.5 km wavelength and longer-wavelength fluctuations could increase the dispersion of the smoke plume. Since this effect is not included in the model runs, the model may underestimate the horizontal dispersion of the smoke plume even though it is modeling the effect of the subgrid-scale eddies correctly.

[23] We can also use the model to explore the time evolution of the circulation induced by the release of sensible heat from the fire. Figure 7 shows selected streamlines of the circulation for the Timbavati smoke plume at 0, 15, 30, 45 and 60 min after the fire ignition. We can see that the buoyancy from the fire source induces a rising circulation below 1 km in altitude, causing the streamlines starting at 0.25 and 0.5 km in altitude (the blue dashed and red dotted lines in Figure 7, respectively) to move upward as we go further in the x direction. This rising motion also induces a low level convergence of surface streamlines, as is shown by the solid black lines in Figure 7. The circulation above 1 km, however, does not appear to be affected by this rising motion.

[24] Figure 8 shows the time evolution of CO mole fractions at 15, 30 and 45 min after fire ignition. Here we also see the general rising motion of the smoke below 1 km,

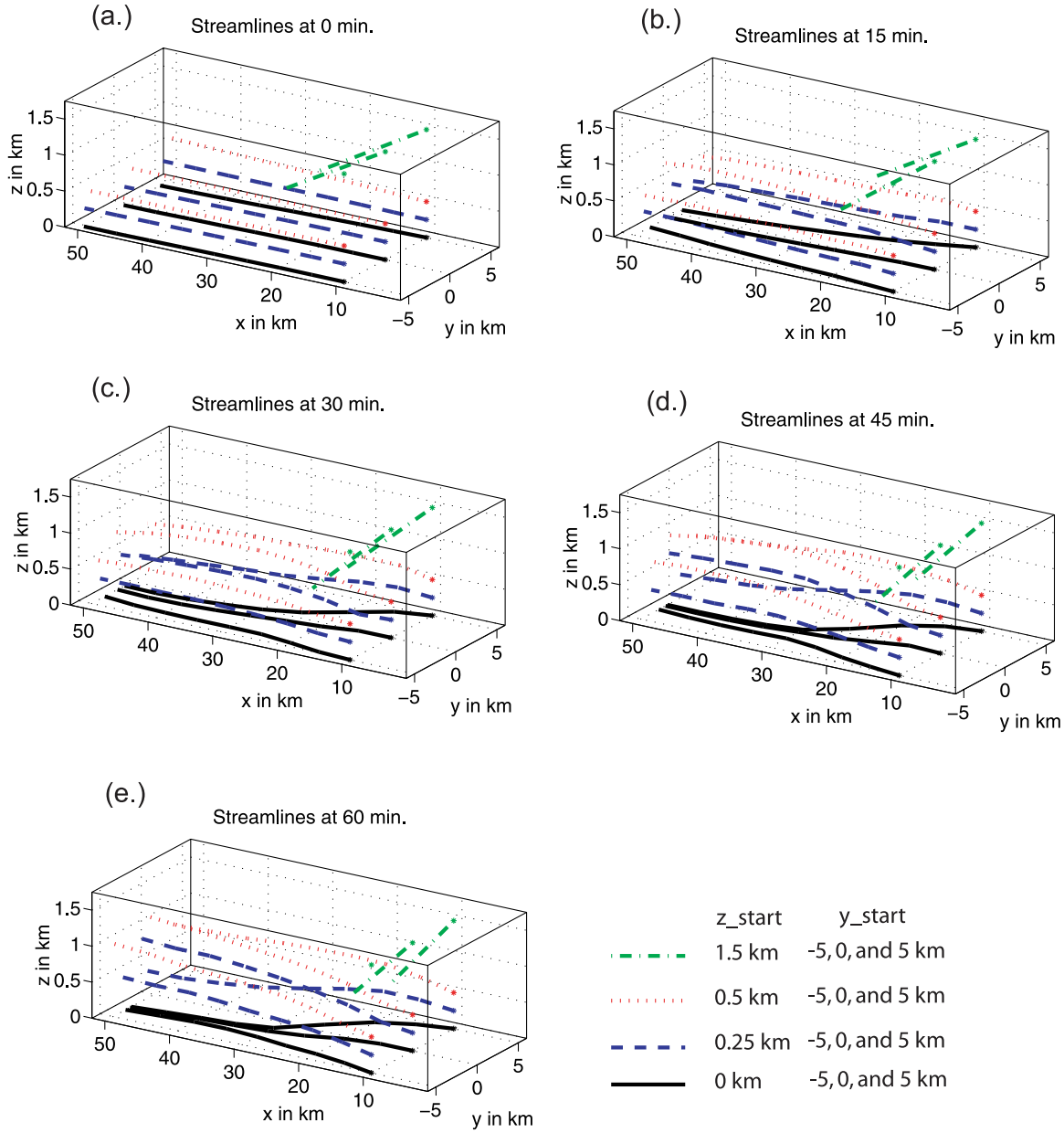

Figure 7. Streamlines for the Timbavati smoke plume simulation. Streamlines are shown every 15 min (K_{min} = 450 m^2/s). All streamlines start at x = 5 km.

along with the horizontal expansion of the smoke plume driven by the higher value of K_{min}.

3.2.2. Ozone, OH, and NO_x

[25] Figure 9 shows the mole fractions or concentrations of O_3, OH, and HONO along the centerline of the smoke plume for both the reference and expanded chemistry cases, while Figure 10 shows the mole fractions or concentrations of these gases along four different horizontal transects through the smoke plume. The maximum ozone concentration for the reference chemistry case (62.3 ppb) is at the bottom of the observed range of ozone concentrations (approximately 60–135 ppb) found downwind in the Timbavati plume [*Hobbs et al.*, 2003]. The expanded chemistry case provides a closer match to the observed ozone concentrations, with a maximum O_3 value of 105.6 ppb. The horizontal transects show that for both cases, the plume mole fraction of O_3 is significantly higher at z = 0.6 km than at z = 1.0 km near the source (x = 16 km), but the mole fraction at z = 1.0 km is higher than that at z = 0.6 km further downwind (x = 36 km). Downwind, the maximum O_3 varies by 5 to 10 ppb with altitude, showing that differences in the sample height can affect the measured O_3 concentration. However, this variation is smaller than the 20 ppb uncertainty of the airborne FTIR measurements of O_3 made for the Timbavati smoke plume [*Yokelson et al.*, 2003].

[26] The higher O_3 mole fractions in the expanded chemistry case are primarily from the heterogeneous production of HONO from NO_2, with the uncharacterized organic species making a smaller contribution. Figures 9

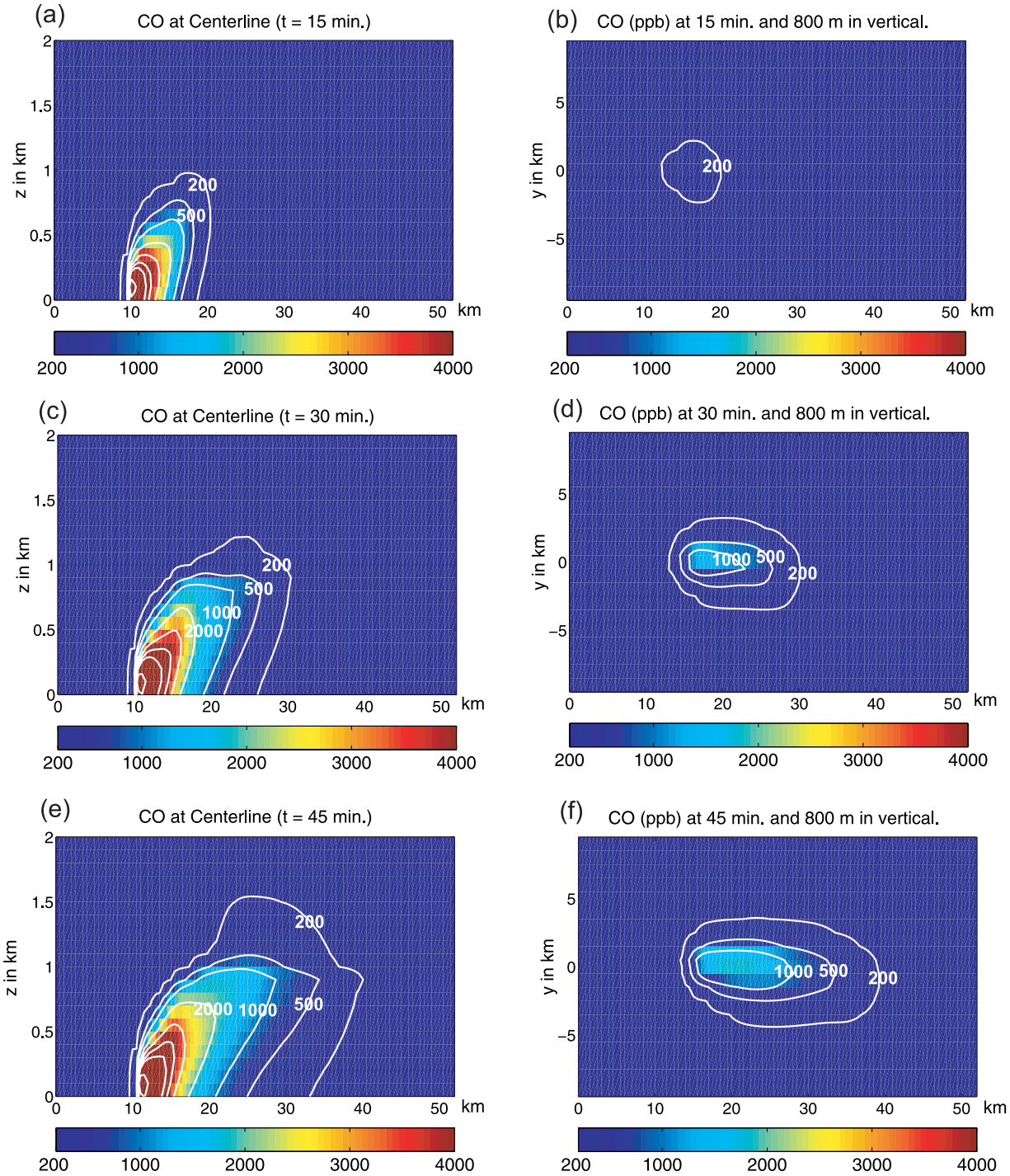

Figure 8. CO mole fractions (ppb) at the centerline (y = 0) and at 800 m in altitude at 15, 30, and 45 min into the integration (K_{min} = 450 m^2/s).

and 10 show the impact of including this heterogeneous reaction on the modeled concentrations or mole fractions of OH and HONO. The maximum OH concentration increases from 7.0×10^6 radicals cm^{-3} to 1.0×10^7 radicals cm^{-3}, but is still well below the inferred plume average value of $1.7(\pm 0.2) \times 10^7$ radicals cm^{-3} reported by *Hobbs et al.* [2003]. In addition, the location of the OH maximum changes. In the reference chemistry case (Figures 9c and 10c), the maximum OH concentrations are found on the edges of the plume. This is because the concentrations of the sinks of OH and the absorption of solar radiation by aerosols are highest in the center of the smoke plume, thereby increasing the destruction of OH while reducing its formation from the photolysis of O_3 and HCHO. In the expanded chemistry case (Figures 9d and 10d), the concentration of OH is highest in the center of the plume near the source, and is relatively constant through the smoke plume further downwind. This is because the heterogeneous pro-

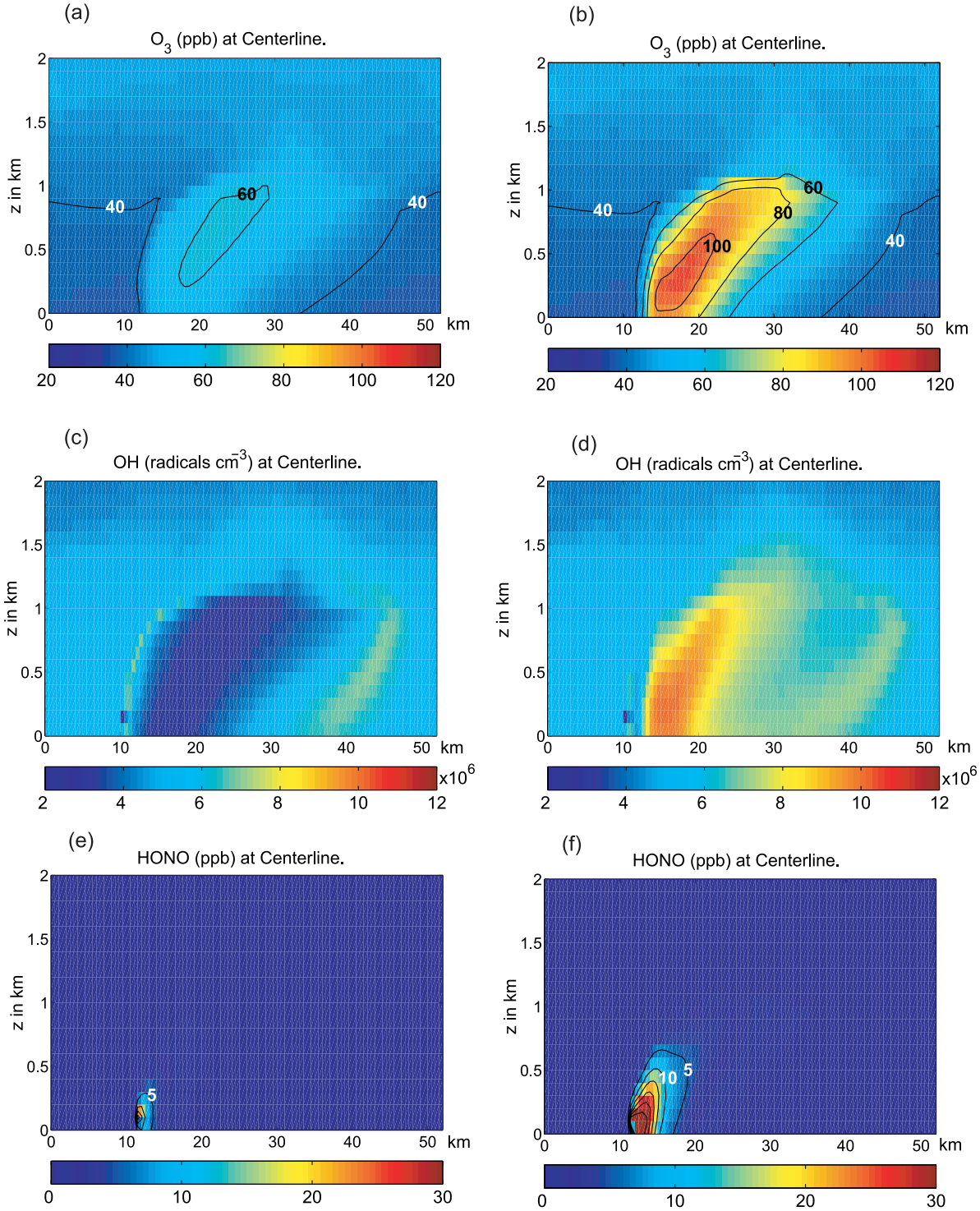

Figure 9. Mole fractions or concentrations of (a and b) O_3, (c and d) OH, and (e and f) HONO along the centerline of the Timbavati smoke plume (y = 0). Figures 9a, 9c, and 9e are for the reference chemistry case, while Figures 9b, 9d, and 9f are for the expanded chemistry case.

duction of HONO is highest in the center of the smoke plume, where the concentrations or mole fractions of NO_2 and aerosol particles are highest. This enhanced HONO production increases the formation of OH in the smoke plume, counteracting the other effects. This suggests that measurements of OH within the smoke plumes could help to determine if the heterogeneous formation of HONO from NO_2 is responsible for the rapid formation of O_3 observed in young biomass burning smoke plumes.

[27] As expected, the concentration of HONO is higher in the expanded chemistry case because of the heterogeneous formation of HONO. However, the rapid photolysis of HONO to OH and NO keeps the concentration of HONO well below the 20 ppb detection limit of the airborne FTIR

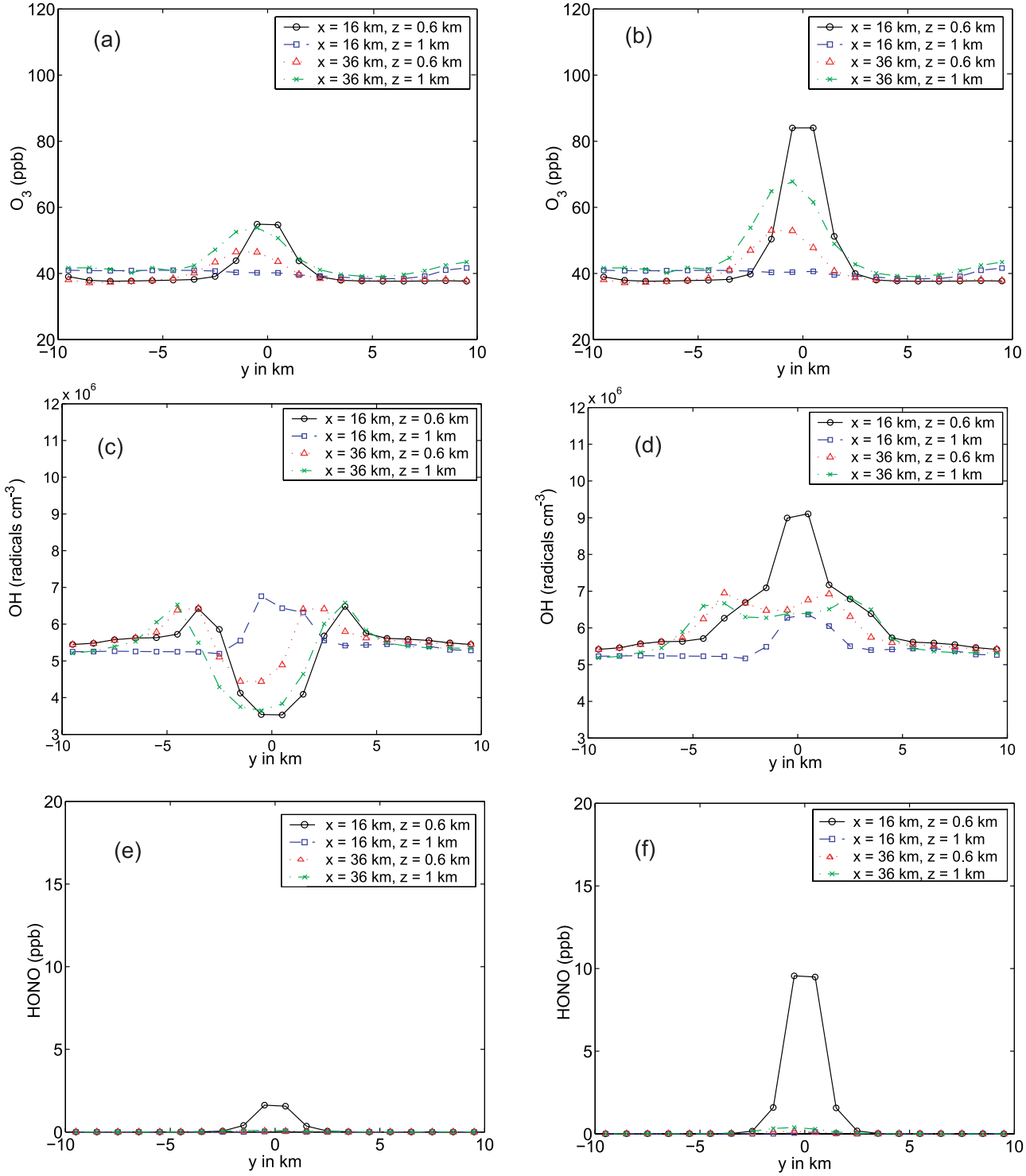

Figure 10. Mole fractions or concentrations of (a and b) O_3, (c and d) OH, and (e and f) HONO along horizontal transects through the Timbavati smoke plume. Figures 10a, 10c, and 10e are for the reference chemistry case, while Figures 10b, 10d, and 10f are for the expanded chemistry case.

measurements made in the Timbavati smoke plume. In addition, the predicted downwind concentrations of HONO are very small, suggesting that direct measurements of HONO in downwind transects of smoke plumes would have to be very sensitive to determine if the heterogeneous formation of HONO were taking place.

[28] Figure 11 shows the mole fractions of NO, NO_2, and NO_x along the centerline of the smoke plume for both the reference and expanded chemistry cases. The mole fractions of NO_x are lower in the expanded chemistry case. This reduction of NO_x is caused by the heterogeneous reaction of NO_2, which increases the formation of HNO_3 directly (since

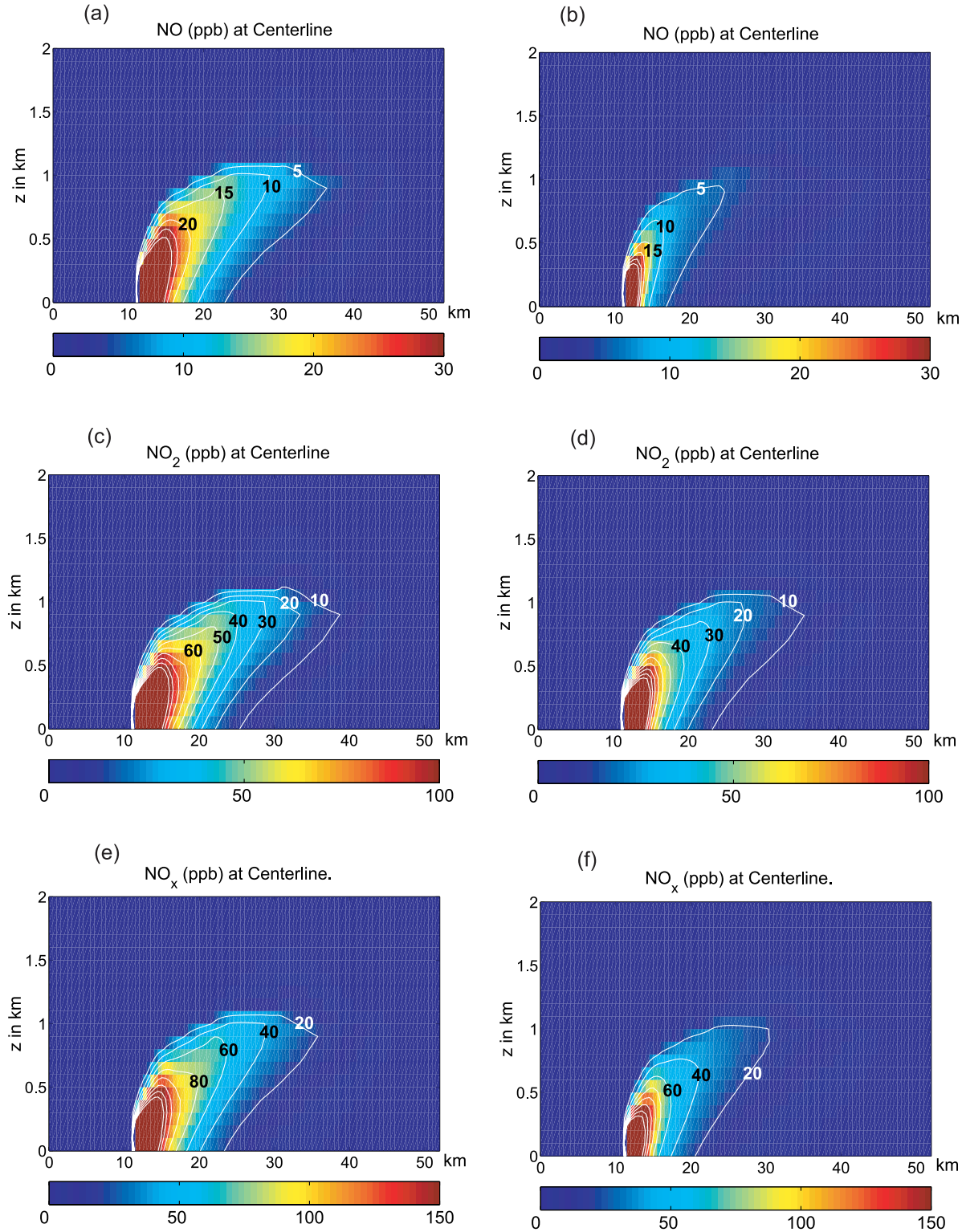

Figure 11. Mole fractions of (a and b) NO, (c and d) NO_2, and (e and f) NO_x along the centerline of the Timbavati smoke plume (y = 0). Figures 11a, 11c, and 11e are for the reference chemistry case, while Figures 11b, 11d, and 11f are for the expanded chemistry case.

1 of every 2 NO_2 molecules that react are converted to HNO_3) and indirectly by increasing the OH concentration, which increases the rate of the gas-phase reaction OH + NO_2 + M → HNO_3 + M. The maximum NO_x mole fractions for both the reference and expanded chemistry are at or below the airborne AFTIR detection limits for NO and NO_2 (20 ppb [*Yokelson et al.*, 2003]), which is consistent with the observations [*Hobbs et al.*, 2003]. At x = 36 km, the

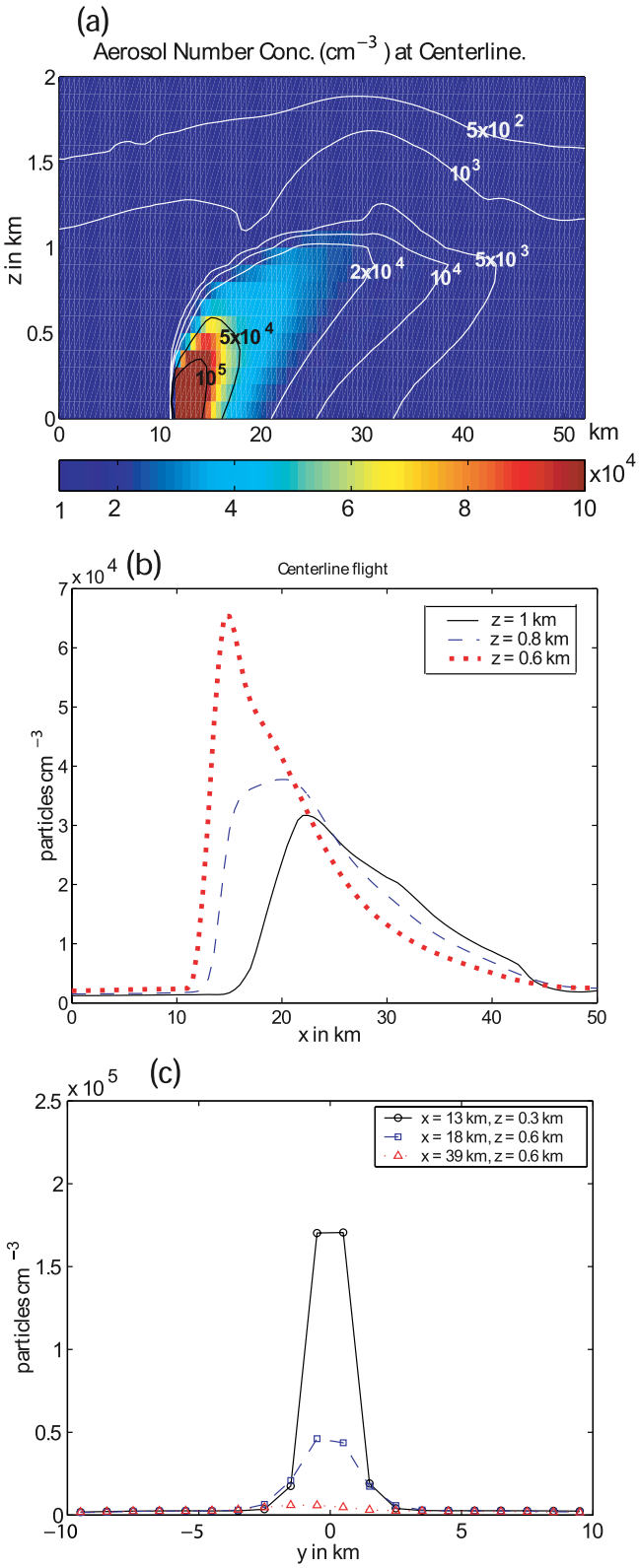

Figure 12. Total aerosol number concentration in the Timbavati smoke plume for the expanded chemistry case: (a) a vertical slice along the plume centerline (y = 0), (b) aerosol number concentration versus downwind distance for different altitudes along the plume centerline, and (c) horizontal transects of the plume.

maximum NO_x for the reference chemistry case is 10.0 ppb and 20.7 ppb at z = 0.6 km and z = 1.0 km, respectively, while the maximum NO_x for the expanded chemistry case is 6.6 ppb and 12.6 ppb, respectively. Thus, the difference between the two cases and the two altitudes are small compared to the 20 ppb uncertainty in the airborne FTIR measurements. This suggests that a NO_x instrument would need a precision of approximately 1–2 ppb to determine if heterogeneous reactions of NO_2 were taking place, and that slight differences in altitude during the transect flights could cause differences of the same order of magnitude. This would make it difficult to use NO_x measurements to determine if heterogeneous NO_x chemistry is taking place.

3.2.3. Aerosol Number Concentrations

[29] Figure 12 shows the total aerosol number concentrations for the expanded chemistry case. The results for the reference case are nearly identical. Figure 12a shows concentrations for a vertical slice through the plume centerline. The second set of plots shows the number concentration versus downwind distance along the centerline at three different altitudes. These plots are designed to mimic the flight path taken by *Hobbs et al.* [2003]. The third set of plots are for three horizontal transects through the smoke plume that were chosen to mimic Samples 2, 3, and 5 of *Hobbs et al.* [2003]; however, the altitudes of the two transects near the source were lowered by 300 m to place them in the center of the modeled plume.

[30] Figure 12b shows a peak at z = 0.6 km of 6.5 × 10^4 particles cm^{-3} near the source, with values at 10 and 20 km downwind (x = 20 and 30 km, respectively) varying between 2.1–4.3 × 10^4 and 1.4–2.2 × 10^4 particles cm^{-3}, respectively, depending on altitude. The measurements of *Hobbs et al.* [2003] showed an aerosol number concentration of 8.8 × 10^4 particles cm^{-3} near the source, decreasing to 3.0 × 10^4 particles cm^{-3} at 10 km downwind from the fire and increasing to 4.5 × 10^4 particles cm^{-3} at 20 km downwind. Thus the modeled aerosol number concentration matches the observations well for the first 10 km downwind, but underestimates the observed aerosol number concentration beyond that distance. This result is similar to the result of our Lagrangian studies, where the Lagrangian model was able to match the initial decrease of number concentration with distance, but could not match the observed increase in number concentration downwind [*Alvarado and Prinn*, 2009]. These Lagrangian studies showed that current nucleation parameterizations would not predict a significant rate of new particle formation in the Timbavati smoke plume, and suggested that the observed increase could be due to the motion of the sampling plane relative to the plume centerline or due to small particles growing by condensation into the detectable size range of the instruments. Figure 12 shows that the aerosol number concentration within the plume can vary significantly with altitude, and falls off rapidly with distance from the plume centerline. This result is consistent with our hypothesis that the reported increase in aerosol particle concentrations with downwind distance may be due to the airplane moving relative to the plume centerline.

3.2.4. Aerosol Mass Concentrations

[31] Figure 13 shows the mass concentrations of potassium (K^+) and black carbon (BC) at the centerline of the smoke plume. These species are not formed or destroyed

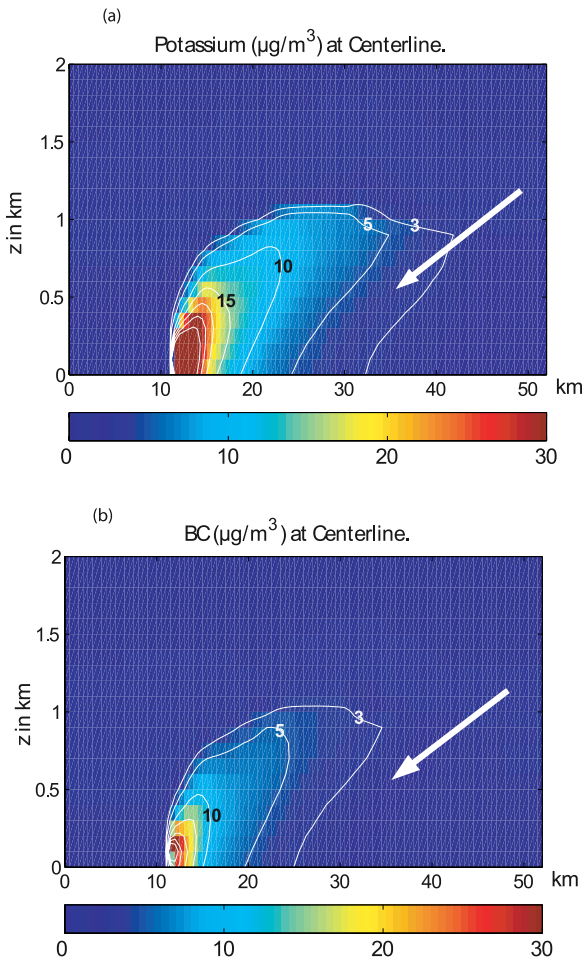

Figure 13. Aerosol mass concentrations of potassium (K^+) and black carbon (BC) at the centerline of the Timbavati smoke plume ($y = 0$). The white arrow points to the location of the downwind aerosol measurement from *Hobbs et al.* [2003]. The observed concentrations at this location for K^+ and BC were 3.8 and 6.7 $\mu g/m^3$, respectively.

within the model, and so act as conservative tracers. Figure 13 shows the results for the expanded chemistry case, which are nearly identical to the reference chemistry case (not shown). The potassium concentration at x = 36 km and z = 0.6 km of 3.5 $\mu g/m^3$ is consistent with the downwind (Sample 5) observation of 3.8 $\mu g/m^3$ reported by *Hobbs et al.* [2003]. As in the Lagrangian studies from *Alvarado and Prinn* [2009], the model underestimates the downwind concentration of BC at this location (modeled at 2.2 $\mu g/m^3$ versus the observed concentration of 6.7 $\mu g/m^3$). As discussed by *Alvarado and Prinn* [2009], this discrepancy may be due to the absorption of solar radiation by secondary organic species, which would cause the observed BC concentration, measured by absorption, to be an overestimate because it includes some of the light-absorbing OC.

[32] Figure 14 shows the mass concentrations of sulfate (SO_4^{2-}) and organic carbon (OC) at the centerline of the smoke plume for the reference and expanded chemistry cases. The expanded chemistry improves the match with observations for these species, but still estimates lower concentrations than reported by *Hobbs et al.* [2003]. For sulfate, *Hobbs et al.* [2003] report a concentration of 8.1 $\mu g/m^3$ for Sample 5, while the model gives concentrations (at x = 36 km and z = 0.6 km) of 4.2 and 5.5 $\mu g/m^3$ for the reference and expanded chemistry cases, respectively. For OC, *Hobbs et al.* [2003] report a concentration of 34 $\mu g/m^3$ for Sample 5, while the model gives concentrations of 13.1 and 14.2 $\mu g/m^3$ for the reference and expanded chemistry cases, respectively. However, it is worth noting that at x = 36 km the maximum concentrations of sulfate and OC occur at z = 1 km, with values of 7.5 $\mu g/m^3$ SO_4^{2-} and 22.7 $\mu g/m^3$ OC, which are closer to the observed concentrations. This suggests that part of the difference between the model and observation may be due to differences in the height of the maximum smoke concentrations downwind.

[33] Figure 15 shows the mass concentrations of chloride (Cl^-) and the mole fractions of HCl gas for the reference and expanded chemistry cases. Close to the fire source, the expanded chemistry case has more of the chloride present in the gas phase as HCl than in the reference chemistry case. This is because more sulfate and nitrate are formed in the expanded chemistry case, and the condensation of these acids onto the aerosol pushes the equilibrium of the chloride toward the gas phase. In both cases, the chloride is almost entirely present in the gas phase at x = 36 km, with aerosol Cl^- concentrations of 0.10 and 0.08 $\mu g/m^3$ for the reference and expanded chemistry cases, respectively. These modeled aerosol Cl^- concentrations are well below the observed downwind Cl^- concentration of 5.4 $\mu g/m^3$. As in the work by *Alvarado and Prinn* [2009], this underestimate of aerosol Cl^- suggests that our aerosol chemical model may not be capturing the correct partitioning between the gas and aerosol phase for inorganic species. The total (gas + aerosol) amount of chloride present in the model at x = 36 km is consistent with the observations, but the model predicts that it should be present largely in the gas phase.

[34] Figure 16 shows the mass concentrations of nitrate (NO_3^-) and the mole fractions of HNO_3 gas for the reference and expanded chemistry cases. The total (gas + aerosol) nitrate concentrations are much higher in the expanded chemistry case than in the reference chemistry case. This is consistent with the increased loss of NO_x in the expanded chemistry case discussed above. The aerosol nitrate concentration at x = 36 km and z = 0.6 km were 1.8 $\mu g/m^3$ and 3.0 $\mu g/m^3$ for the reference and expanded chemistry cases, respectively. These values are much lower than the concentration of 9.1 $\mu g/m^3$ reported by *Hobbs et al.* [2003]. The total nitrate concentration at x = 36 km and z = 0.6 km in the expanded chemistry case is below the reported aerosol nitrate value. As was the case for sulfate and OC, the maximum gas and aerosol nitrate concentrations at x = 36 km occur at z = 1 km (4.4 ppb and 6.1 $\mu g/m^3$, respectively) which are closer to observations.

3.2.5. Aerosol Optical Properties

[35] Figure 17 shows the aerosol scattering coefficient and single scattering albedo at the plume centerline as well as the horizontal distribution of aerosol optical depth for the reference and expanded chemistry cases. For the expanded chemistry case, the maximum value near the source (x = 13 km, z = 0.3 km) is 1.5×10^{-3} m^{-1}, decreasing to a value of 7.7×10^{-4} m^{-1} (x = 18 km, z = 0.6 km) and 1.1×10^{-4} m^{-1} downwind (x = 39 km, z = 0.6 km). *Hobbs et al.* [2003]

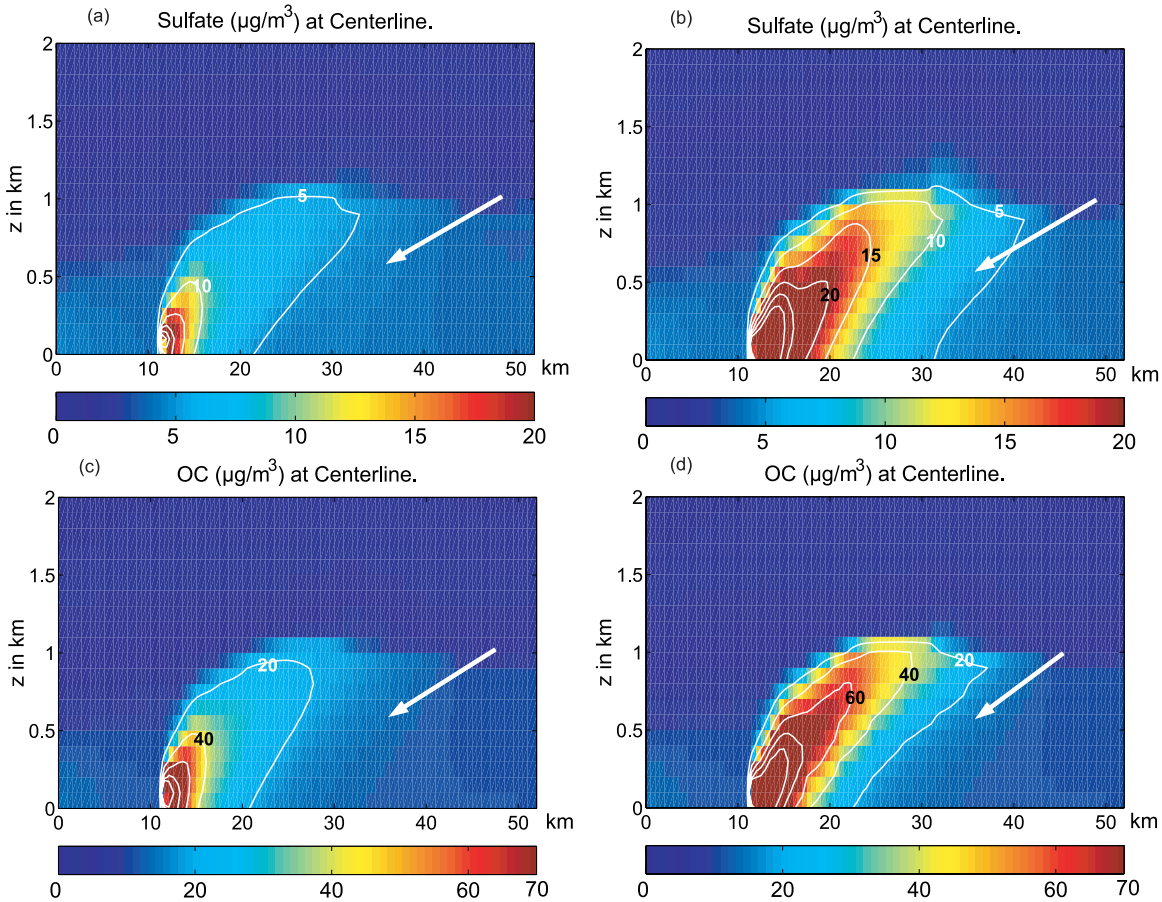

Figure 14. Aerosol mass concentrations of sulfate (SO_4^{2-}) and organic carbon (OC) at the centerline of the Timbavati smoke plume (y = 0). The white arrow points to the location of the downwind aerosol measurement from *Hobbs et al.* [2003]. The observed concentrations at this location for SO_4^{2-} and OC were 8.1 and 34 μg/m^3, respectively.

reported a peak value of 2.2×10^{-3} m^{-1} for the light scattering coefficient near the source, decreasing to 7.5×10^{-4} m^{-1} at 5 km downwind and to 4.0×10^{-4} m^{-1} at 26 km downwind. These results are similar to the results for the total aerosol number concentration, in that the model is able to reproduce the observed decrease in aerosol scattering coefficient in the first 5 to 10 km downwind, but then underestimates the value further downwind. Thus, the underprediction of the scattering coefficient downwind is likely due to the underprediction of the downwind number concentration.

[36] The aerosol single scattering albedo is larger in the expanded chemistry case than in the reference chemistry case, because of the larger condensation rate of secondary organic and inorganic species onto the aerosol in the expanded chemistry case. The maximum single scattering albedo predicted for the expanded chemistry case is 0.906, near the top of the range of 0.86 ± 0.05 reported by *Reid et al.* [2005a] for aged grassland and savannah smoke. This leads to a larger aerosol scattering coefficient for the expanded chemistry case as well. The aerosol optical depth is also larger for the expanded chemistry case, as the particles have a larger optical cross section than in the reference chemistry case.

3.2.6. Solar Radiation and Photolysis Rates

[37] Figure 18 shows the total solar irradiance (the sum of both the upward and downward streams, integrated over 0–4 μm in wavelength), the heating rate due to the absorption of solar radiation, and the NO_2 photolysis rate along the plume centerline for the reference and expanded chemistry cases. The values for all three parameters are very similar for the two chemistry cases, with the expanded chemistry case showing a slightly larger upward diffuse irradiance above the plume due to the higher aerosol scattering coefficient in this case. The total solar irradiance is increased above the smoke plume because of the scattering of solar radiation by the smoke aerosols, which increases the upward diffuse irradiance. The solar irradiance within and below the smoke plume is decreased, because of the increased scattering and absorption of solar radiation within the smoke plume, which reduces the upward and downward flux of solar radiation within and beneath the smoke plume. The magnitudes of the increases and decreases of the solar irradiance are approximately 10–20%. *Hobbs et al.* [2003] reported that the UV flux in the wavelength band 300–390 nm in the center of the plume was about two thirds of that near the top of the plume. As the smallest wavelength band in our radiation module is from 0 to 700 nm, we

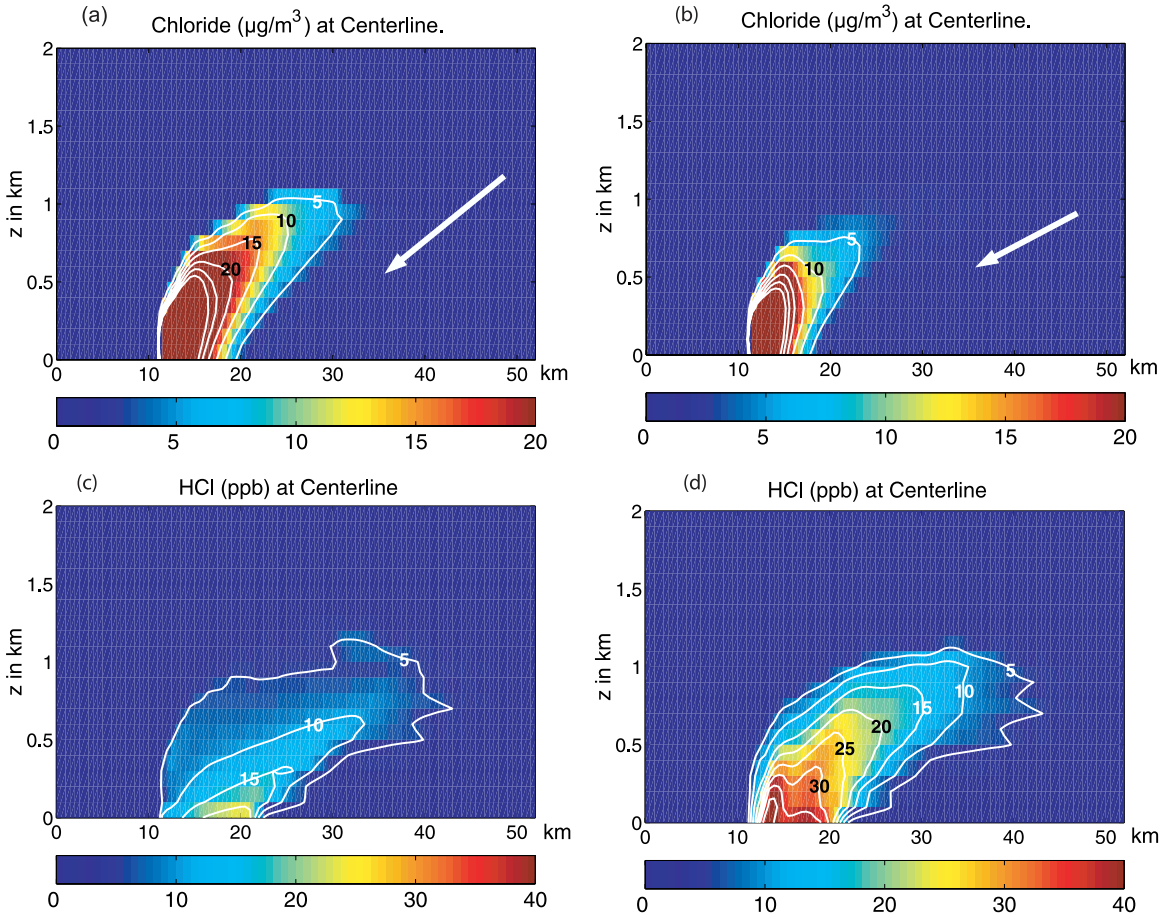

Figure 15. (a and b) Concentrations of aerosol chloride (Cl^-) and (c and d) mole fractions of gas-phase HCl at the centerline of the Timbavati smoke plume ($y = 0$). Figures 15a and 15c are for the reference chemistry case, while Figures 15b and 15d are for the expanded chemistry case. The white arrow points to the location of the downwind aerosol measurement from *Hobbs et al.* [2003]. The observed Cl^- concentration at this location was 5.4 $\mu g/m^3$.

cannot directly compare our model results to this observation. However, the minimum (916 W/m^2) solar irradiance shown in Figure 18b is 77% of the maximum irradiance (1196 W/m^2). This suggests that the model may be slightly underestimating the absorption of solar radiation by the aerosols in the wavelength band 300–390 nm. This additional absorption may be due to secondary organic compounds that absorb radiation, which would also help to explain the underestimate of BC relative to observations.

[38] *Hobbs et al.* [2003] estimated an instantaneous heating rate of the plume of 7.4 K/d at 20–25 km downwind from the Timbavati fire due to the absorption of solar radiation within the smoke plume, on the basis of their measurements of upwelling and downwelling solar irradiance within the plume. Figures 18c and 18d show the solar heating rates predicted for our model simulations. At 20–25 km downwind, the modeled heating rate varies from 4 to 6 K/d, which is slightly lower than the reported value. This is consistent with the observations of BC and UV flux, which also suggest that the model may slightly underestimate the absorption of solar radiation by the smoke aerosols.

[39] Figures 18e and 18f show the NO_2 photolysis rate predicted for the two chemistry cases. The spatial patterns are very similar to the spatial patterns for solar irradiance, with the photolysis rate being decreased within and below the smoke plume and increased above. These increases and decreases are on the order of 10–20%, which is of similar magnitude to the parametric uncertainty of the NO_2 photolysis reaction (±30% [see *Pun*, 1998]).

4. Comparison to Automatic Dilution Approach

[40] Here, we estimate the errors caused by the automatic dilution approach of GACMs by comparing the results of our 3-D Eulerian simulation of the Timbavati smoke plume to the results of the single-box Eulerian model described in section 2.2. This Eulerian box model is used as an analog of the large-scale grid boxes of GACMs. Section 4.1 describes the initial conditions and model parameters for the box model simulation of the Timbavati fire. Section 4.2 discusses the results of the comparison between the box and 3-D models for the species CO, O_3, NO_x, other NO_y species, and aerosols.

4.1. Box Model Initialization

[41] The temperature and pressure for the box model were set at 288 K and 900 mbar, respectively. The horizontal

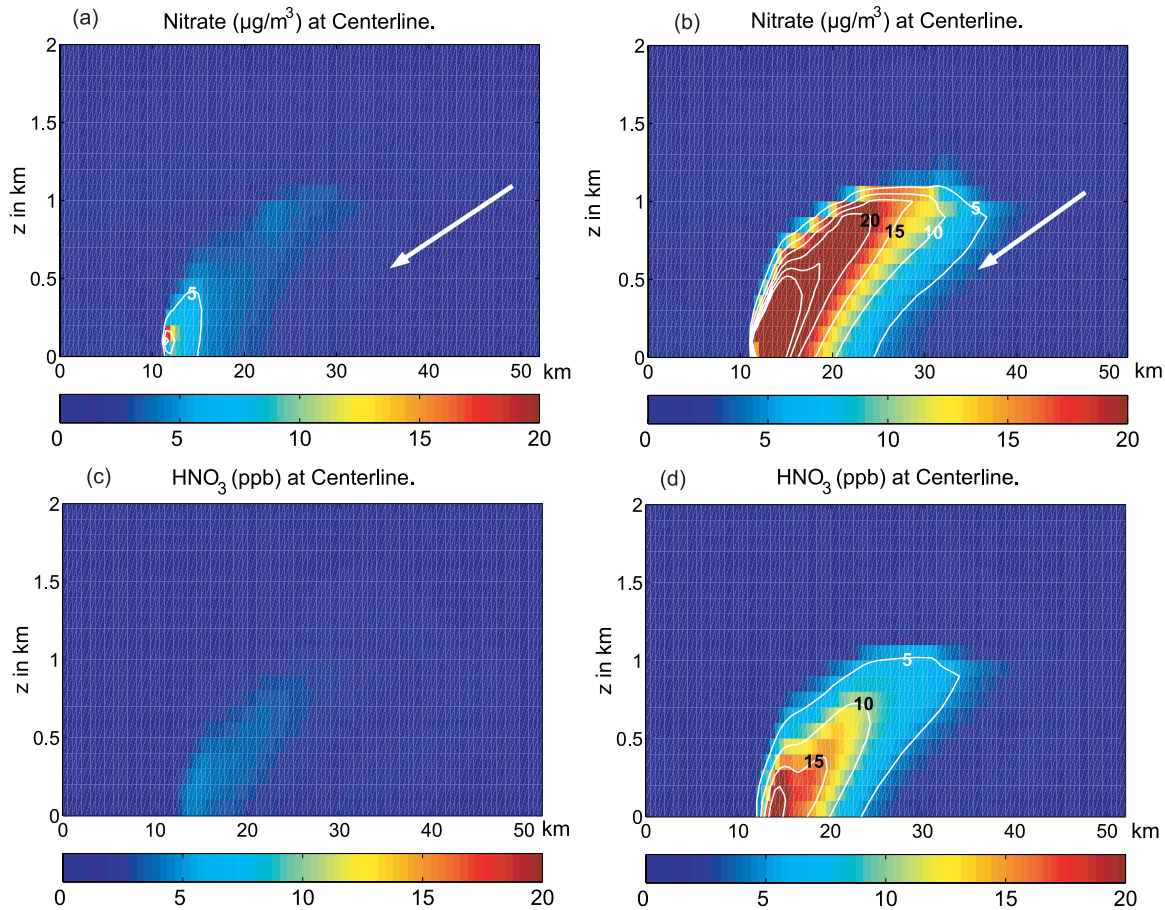

Figure 16. (a and b) Concentrations of aerosol nitrate (NO_3^-) and (c and d) mole fractions of gas-phase HNO_3 at the centerline of the Timbavati smoke plume ($y = 0$). Figures 16a and 16c are for the reference chemistry case, while Figures 16b and 16d are for the expanded chemistry case. The white arrow points to the location of the downwind aerosol measurement from *Hobbs et al.* [2003]. The observed NO_3^- concentration at this location was 9.1 μg/m^3.

wind speed was set at 9.3 m/s [*Trentmann et al.*, 2005]. The horizontal domain of the Eulerian box is the same as the model domain for the 3-D Eulerian plume studies of section 3.

[42] Photolysis rates were calculated using TUV v.4.1, and are the same as the rates used in the Lagrangian study of *Alvarado and Prinn* [2009]. Table 1 compares the photolysis rates calculated by the CRM6 model and TUV v.4.1. The photolysis rates calculated by the two methods are generally within 25%, with CRM6 giving lower values due to a slightly lower estimate of the actinic flux. An error of 25% is on the same order as the parametric uncertainty for these photolysis reactions [*Pun*, 1998]. The two exceptions are the reactions $NO_3 \rightarrow NO + O_2$ and $HCHO \rightarrow H_2 + CO$, where the CRM6 calculated values are only 65% and 51%, respectively, of the TUV calculated values. However, these reactions are unlikely to have a significant impact on the chemistry. The concentration of NO_3 is very low in the daytime and the other photolysis pathway for NO_3 is dominant. For the second HCHO pathway, H_2 and CO are fairly unreactive on the 1 h time scale of interest here, and so should not significantly impact the chemistry within the smoke plume.

[43] Initial and upwind concentrations of gases other than SO_2 and O_3 were set to the background concentrations for Timbavati as given by *Alvarado and Prinn* [2009]. Since the concentrations of SO_2 and O_3 varied with height in the bottom 1 km in the 3-D model domain (see Figure 4), the initial and upwind concentrations were set to the average values of 1.45 ppb and 35.7 ppb, respectively, to match the total amount of SO_2 and O_3 initially present in the bottom 1 km of the 3-D model. Similarly, the initial and upwind number concentration of aerosols was set at 2530 cm^{-3} to match the average aerosol concentration present in the bottom 1 km of the 3-D model (see Figure 5). As in the 3-D modeling, 4 aerosol size bins were used in the box model, with 2 bins between 0.015 μm and 1 μm in radius. Initial and upwind aerosol chemical compositions were taken from the environmental aerosol distribution concentrations for Timbavati listed in part 1 [*Alvarado and Prinn*, 2009]. The emissions of trace gases and aerosols due to the fire source were identical to the emissions for the 3-D Eulerian model.

[44] The box model was run for the reference and expanded chemistry cases discussed above. The results of both simulations, and their comparison to the 3-D Eulerian plume model results, are presented below.

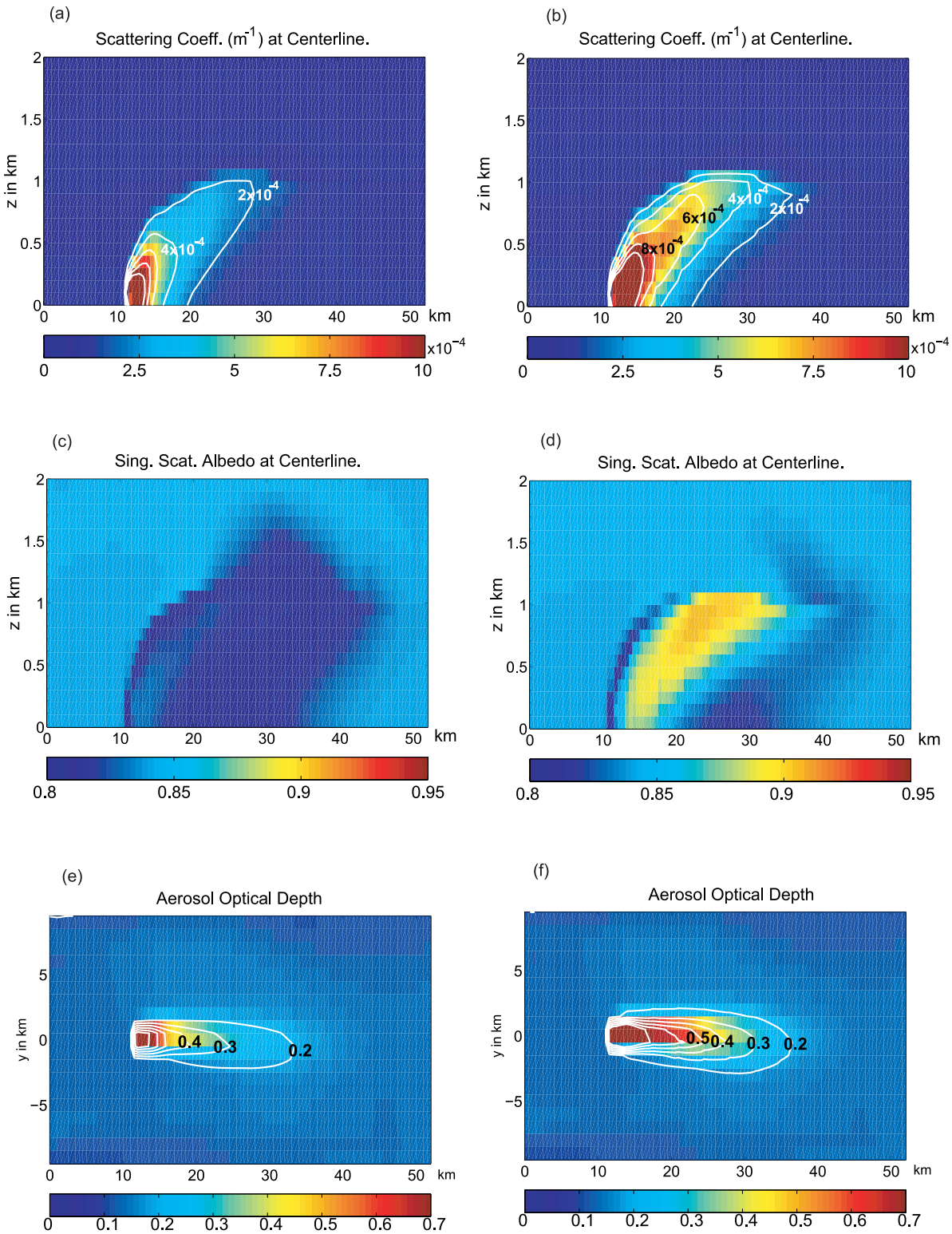

Figure 17. Aerosol optical properties at 550 nm for the Timbavati smoke plume. (a and b) The aerosol scattering coefficient at the plume centerline ($y = 0$). (c and d) The aerosol single scattering albedo at the plume centerline. (e and f) The aerosol optical depth versus x and y. Figures 17a, 17c, and 17e are for the reference chemistry case, while Figures 17b, 17d, and 17f are for the expanded chemistry case.

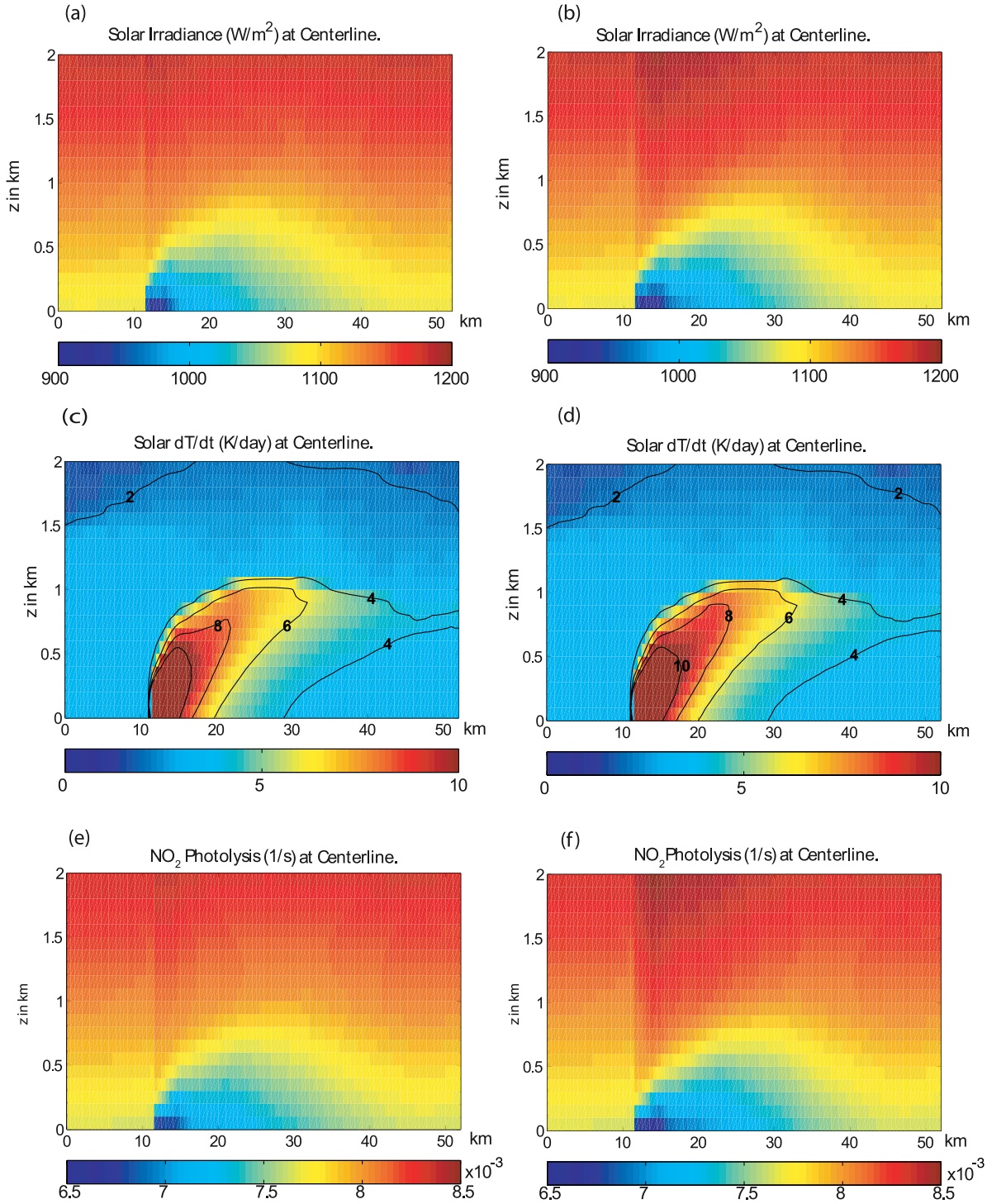

Figure 18. (a and b) The solar irradiance (integrated over wavelengths from 0 to 4 μm), (c and d) the rate of temperature change due to absorption of solar radiation, and (e and f) the NO_2 photolysis rates. Figures 18a, 18c, and 18e are for the reference chemistry case, while Figures 18b, 18d, and 18f are for the expanded chemistry case.

4.2. Results and Discussion

[45] In order to compare the results of the Eulerian box and 3-D models, we define $M_{q,Box}$ (t) as the total amount of species q (in mol) present in the Eulerian box model at time t and define $M_{q,3D}$ (t) as the total amount of species q present in the bottom 1 km of the 3-D Eulerian plume model at time t. $M_{q,Box}$ (t) is calculated from the concentration C_q (t) (mol/cm^3) by the formula

$$M_{q,Box}(t) = C_q(t)\Delta X \Delta Y H \quad (1)$$

where ΔX = 52.5 km, ΔY = 20 km, and H = 1 km.

Table 1. Photolysis Rates Calculated by TUV and CRM6[a]

Reaction	CRM6 (Zenith = 43.53°)	TUV v4.1 (Zenith = 43.4°)	CRM6/TUV
NO_2	7.21×10^{-3}	7.76×10^{-3}	92.9%
$O_3 \rightarrow O\ (^1D)$	2.02×10^{-5}	2.39×10^{-5}	84.5%
$O_3 \rightarrow O\ (^3P)$	4.18×10^{-4}	3.84×10^{-4}	108.8%
H_2O_2	4.86×10^{-6}	5.96×10^{-6}	81.5%
$NO_3 \rightarrow NO + O_2$	1.28×10^{-2}	1.96×10^{-2}	65.3%
$NO_3 \rightarrow NO_2 + O$	1.49×10^{-1}	1.53×10^{-1}	97.4%
HONO	1.59×10^{-3}	1.71×10^{-3}	93.0%
MGLY	8.73×10^{-5}	9.17×10^{-5}	95.2%
CH_3CHO	3.79×10^{-6}	4.58×10^{-6}	82.8%
$CH_3C(O)CH_3$	4.18×10^{-7}	5.44×10^{-7}	76.8%
$HCHO \rightarrow 2\ HO_2 + CO$	1.99×10^{-5}	2.62×10^{-5}	75.9%
$HCHO \rightarrow H_2 + CO$	2.03×10^{-5}	4.00×10^{-5}	50.8%

[a]Rates are in s^{-1}. Photolysis rates calculated for Timbavati fire location at 1 km in altitude. Effect of aerosol on the radiative field was not included.

$M_{q,3D}$ (t) is calculated from the sum

$$M_{q,3D}(t) = \sum_{i=1}^{105} \sum_{j=1}^{20} \sum_{k=1}^{10} C_q(i,j,k,t)\Delta x \Delta y \Delta z \qquad (2)$$

where C_q (i, j, k, t) is the concentration of species q (mol/cm^3) in grid box (i, j, k) at time t, Δx = 500 m, Δy = 1000 m, and Δz = 100 m. Note that $\frac{M_{q,3D}(t)}{\Delta X \Delta Y H}$ is the average concentration of species q in the bottom 1 km of the 3-D plume model at time t.

[46] For both the box and 3-D models, M_q can be changed by emissions of species q by the fire, reversible and irreversible chemical reactions, and by horizontal transport. $M_{q,3D}$ can also change because of vertical diffusion of species into or out of the bottom 1 km of the 3-D model. In order to estimate the error in the effective flux of biomass burning emissions to the global environment caused by the automatic dilution of emissions in the box model, we calculate the change in M_q in both models from the ignition of the fire source (t = 0) to the end of the model integration (t = 60 min):

$$\Delta M_q = M_q(60\text{min}) - M_q(0) \qquad (3)$$

[47] Note that $\frac{\Delta M_q}{\Delta X \Delta Y H}$ represents the change in the average concentration over 60 min of fire emissions.

[48] The bar graphs presented in sections 4.2.1 through 4.2.4 plot ΔM_q for the reference and expanded chemistry runs of the Eulerian box and 3-D models. The percentages shown above the bars for the box model represent the normalized difference (ε_q) between the box and 3-D model results, calculated using the formula

$$\varepsilon_q = \frac{\Delta M_{q,Box} - \Delta M_{q,3D}}{\Delta M_{q,3D}} \qquad (4)$$

[49] Since both models are spun up for 10 min prior to fire ignition, $M_{q,Box}$ (0) and $M_{q,3D}$ (0) can be different. The error bars in Figures 19–23 represent the differences (δ_q) between the box and 3-D model amounts of each species at the fire ignition, calculated according to the formula

$$\delta_q = M_{q,Box}(0) - M_{q,3D}(0) \qquad (5)$$

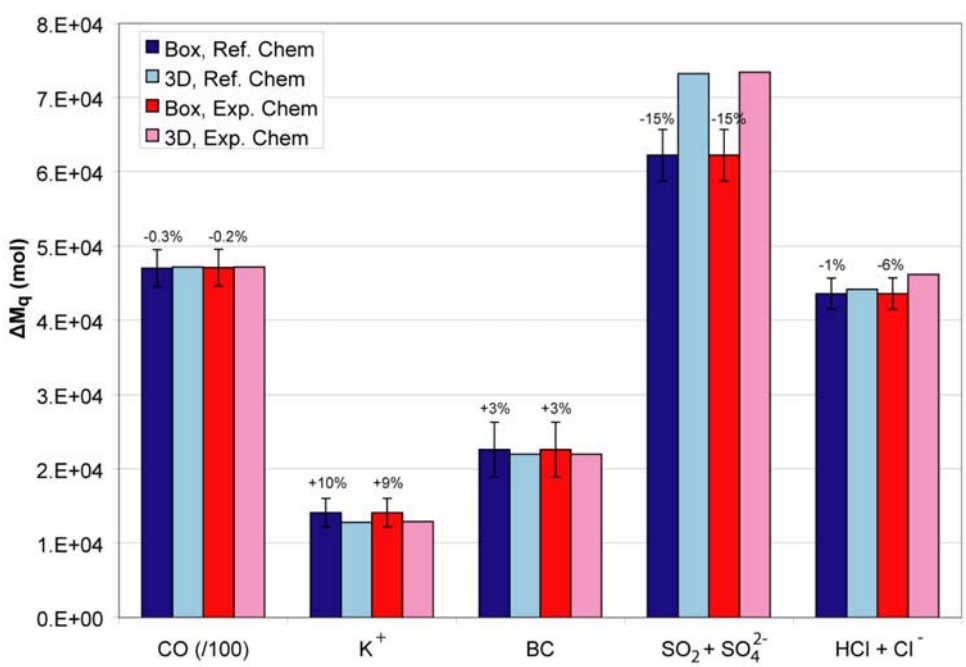

Figure 19. Comparison of Eulerian box and 3-D model results for conservative tracers. Values plotted represent the change in the total amount of a species (mol) in the lowest 1 km of the model domain from the ignition of the fire source to 60 min after ignition (ΔM_q). Error bars represent the differences between the box and 3-D model amounts of each species at the fire ignition (δ_q). The percentages represent the normalized difference of the box model result from the corresponding 3-D model result (ε_q). The values for CO have been divided by 100 to fit in the plot.

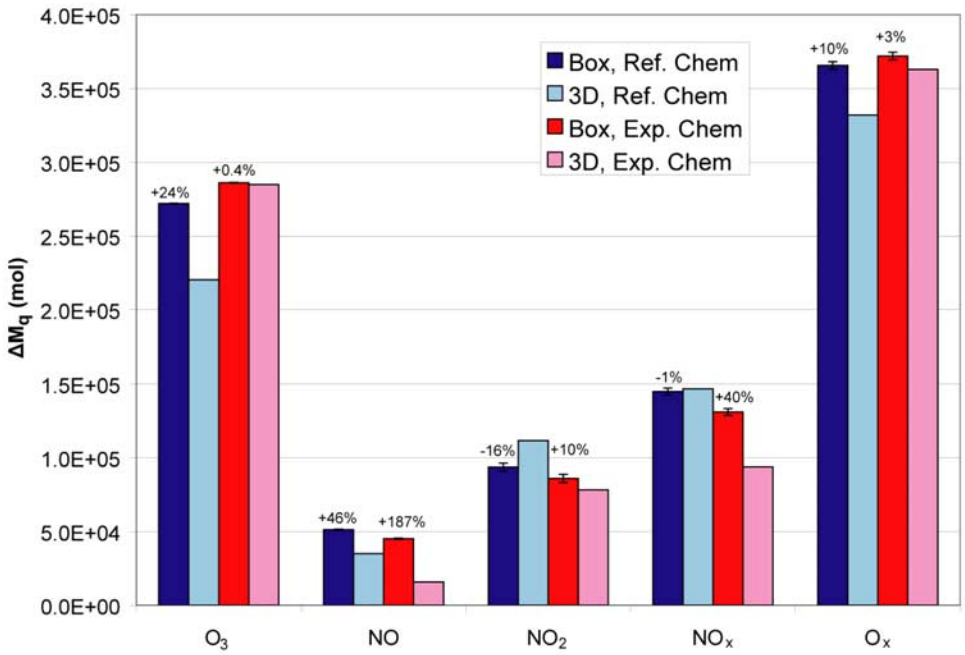

Figure 20. Comparison of Eulerian box and 3-D model results for O_3, NO, NO_2, NO_x (NO + NO_2), and O_x (NO_2 + O_3). Plotted values are the same as described in Figure 19.

4.2.1. Tracers

[50] As mentioned above, the Eulerian box model does not include the vertical diffusion of species across the top boundary, while the 3-D plume model does allow species to diffuse vertically. This can result in differences in $\Delta M_{q,Box}$ and $\Delta M_{q,3D}$ even in the absence of nonlinear chemistry. To evaluate the importance of this effect, we compared $\Delta M_{q,Box}$ and $\Delta M_{q,3D}$ for various tracer species (i.e., for species whose concentrations are not greatly affected by chemical changes in the model).

[51] Figure 19 shows the comparison between the Eulerian box model and the 3-D Eulerian plume model for five tracer species: CO, aerosol potassium (K^+), aerosol black carbon (BC), and the total amount of S and Cl atoms (totals calculated as the sum of the gas and aerosol phase species containing these atoms, namely $SO_{2(g)}$ and aerosol sulfate

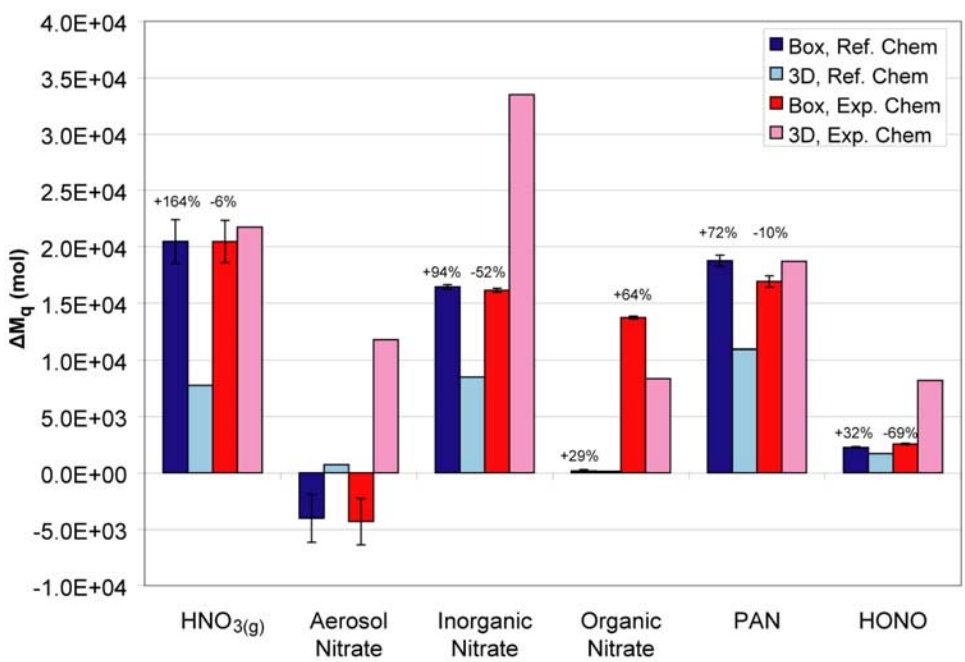

Figure 21. Comparison of Eulerian box and 3-D model results for NO_y species. Plotted values are the same as described in Figure 19.

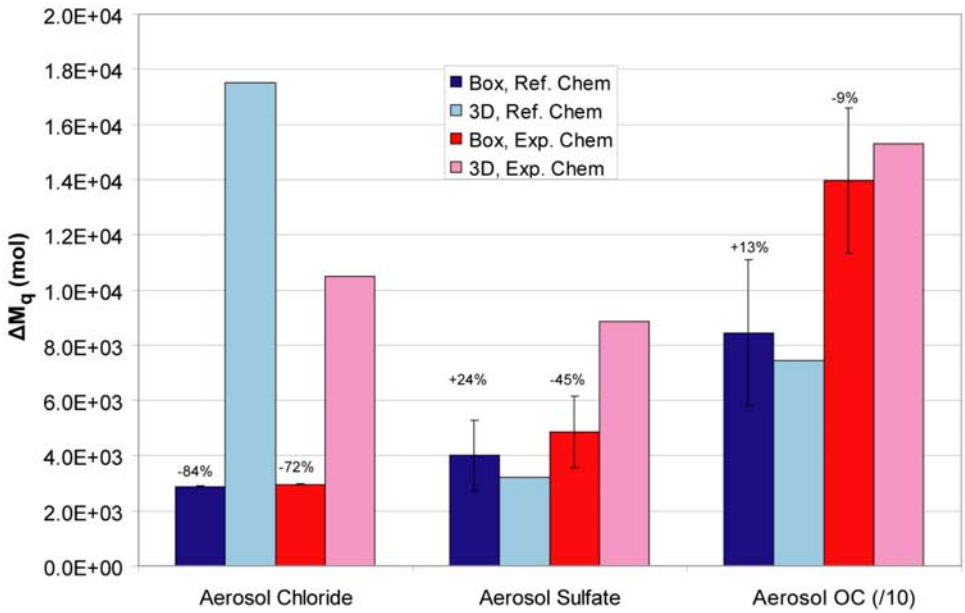

Figure 22. Comparison of Eulerian box and 3-D model results for aerosol chloride, sulfate, and organic carbon (OC). Plotted values are the same as described in Figure 19. The values for OC have been divided by 10 to fit in the plot.

(SO_4^{2-}) and $HCl_{(g)}$ and aerosol chloride (Cl^-), respectively). While CO is not strictly a conservative tracer in the model, the chemical production and loss rates for CO over the model integration times are very small compared to the fire emission rates considered here.

[52] The calculated changes in CO in the box and 3-D models are nearly identical for both chemistry cases studied, with a maximum $|\varepsilon_{CO}|$ of 0.3%. This close correspondence between the box and 3-D models suggests that vertical diffusion of CO across the z = 1 km boundary is unimportant for this species, because of its relatively high background mole fraction (182 ppb) leading to a small vertical CO gradient. For K^+ and BC, $\Delta M_{q,Box}$ is greater than $\Delta M_{q,3D}$. This is due to the upward vertical diffusion of these species in the 3-D model runs. Since the initial aerosol concentrations in the 3-D model decay exponentially with height (i.e., their vertical gradients are large), turbulence causes these species to mix upward, reducing the concentrations below 1 km. Thus we see that the neglect of vertical diffusion in the box model can lead to positive values of ε_q of up to +10% for aerosol species even in the absence of chemical sources and sinks. The change in the total amount of S atoms ($SO_{2(g)}$ + SO_4^{2-}) is lower in the box model than in the 3-D model. This is because the high initial concentration of $SO_{2(g)}$ above 1 km in the 3-D model (see Figure 4) results in a large downward diffuse flux of SO_2 across the z = 1 km boundary. This downward flux of SO_2 compensates for the upward flux of aerosol sulfate, resulting in a negative value for $\varepsilon_{SO2(g)+SO_4^{2-}}$. The total amount of Cl atoms ($HCl_{(g)}$ + Cl^-) is slightly ($\varepsilon_{HCl(g)+Cl^-}$ = −1% to −6%) smaller in the box model than in the 3-D model. The difference between the reference and expanded chemistry results for Cl atoms in the 3-D model is likely due to numerical error in solving the advection-diffusion equations for a species with a very low background concentration (~1 ppt) and a very high concentration gradient near the fire source.

[53] Thus, we find that vertical diffusion alone can result in differences of the order of ±1−15% between the box and 3-D Eulerian model. The values are larger for species with large vertical gradients in their initial concentrations in the 3-D model, such as aerosol species and $SO_{2(g)}$. Thus, we cannot necessarily attribute differences of less than 10 to 15% to the automatic dilution assumption of GACMs. Changes of this size may be due to any combination of vertical diffusion and the error associated with automatically diluting biomass burning emissions.

4.2.2. Ozone and NO_x

[54] Figure 20 shows the comparison between the box and 3-D models for O_3, NO, NO_2, NO_x (NO + NO_2) and O_x (defined here as NO_2 + O_3). When both models are using the reference chemistry, the models give nearly identical results for NO_x (ε_{NOx} = −1%), but the box model gives a higher value for NO (ε_{NO} = +46%) and a lower value for NO_2 (ε_{NO2} = −16%). The differences for NO and NO_2 are consistent with a higher average photolysis rate for NO_2 in the box model. The box model shows larger increases for O_3 (ε_{O3} = +24%) and O_x (ε_{Ox} = +10%) than are seen in the 3-D model. This suggests that, when using the reference chemistry, the box model approach results in a more oxidizing atmosphere than in the 3-D plume model. This result can be explained by referring to the OH transect plots in Figure 10. For the 3-D reference chemistry case, the OH concentration drops in the center of the smoke plume, because of the high concentration of OH sinks and the absorption of solar UV radiation by the smoke aerosols. In the box model reference chemistry case, the sinks of OH are more dilute because of the automatic dilution of smoke emissions and the absorption of solar radiation by the aerosols is ignored. The more dilute sinks of OH result in a higher total amount of OH in the box ($M_{OH,Box}$ (60 min) =

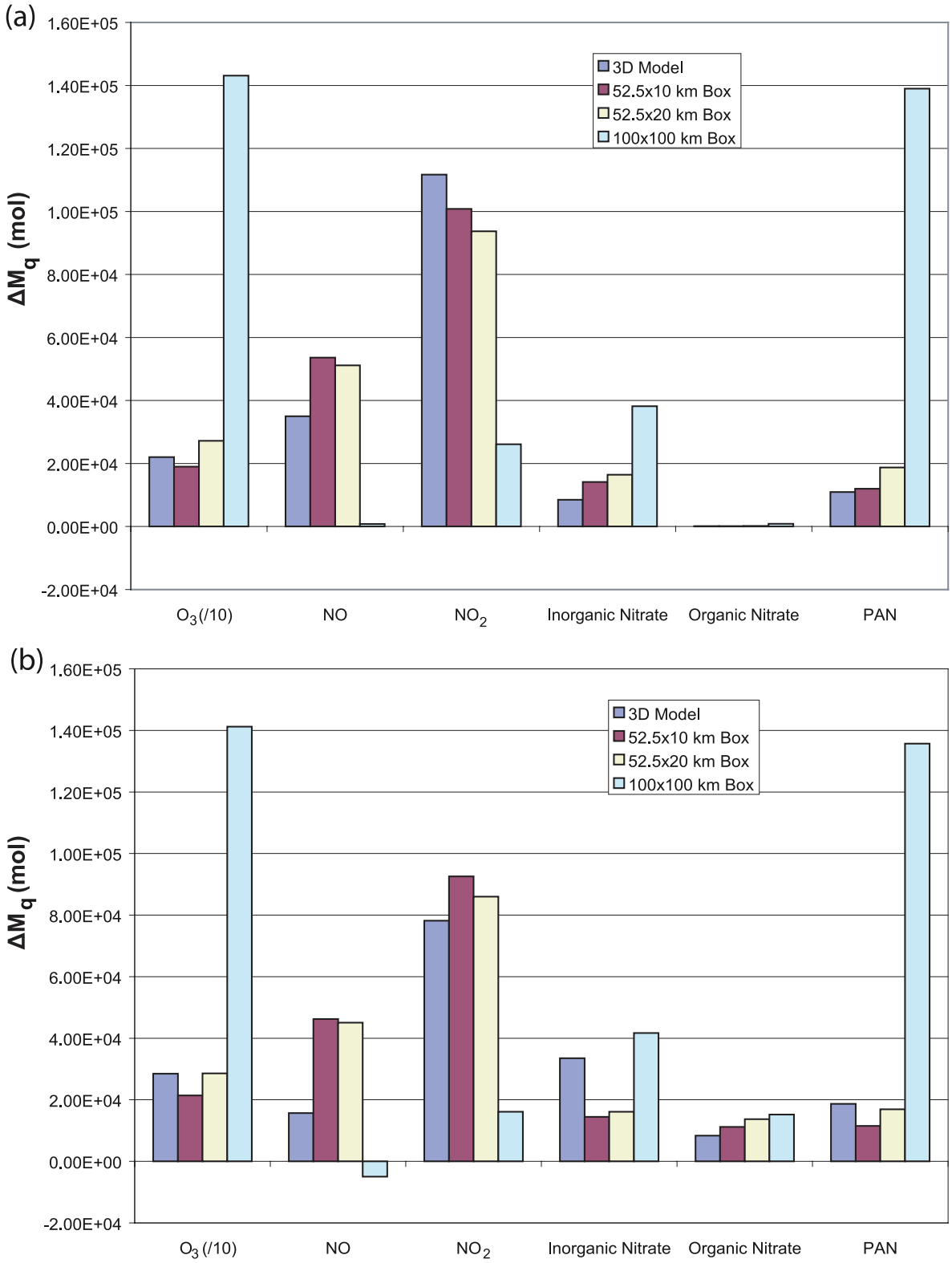

Figure 23. Comparison of 3-D model results with different size Eulerian box models for the (a) reference and (b) expanded chemistry cases. Plotted values are the same as described in Figure 19. O_3 values are divided by 10 to fit on the plot.

14.06 mol) than in the 3-D model ($M_{OH,3D}$ (60 min) = 9.61 mol), while the higher rate of NO_2 photolysis in the box model results in more of the created O_x being present as O_3 in the box model than in the 3-D model. This result is also consistent with the work of *Lin et al.* [1988], who found that the ozone production efficiency (net ozone production per molecule of NO_x lost) decreased as the NO_x concentration increased from 1 ppb (as in the box

model) to 10 ppb or higher (as in the 3-D plume model). Thus, given the similar loss rates of NO_x in both the box and 3-D models, we expect a higher O_3 production rate in the box model.

[55] For the expanded chemistry case, the models match closely for O_3 (ε_{O_3} = +0.4%) and O_x (ε_{O_x} = +3%). However, the box model gives a much higher value for NO_x than the 3-D model (ε_{NO_x} = +40%). This suggests that, for the expanded chemistry case, the automatic dilution of smoke plume emissions results in an overestimate of effective NO_x emissions into the free troposphere from biomass burning sources. This is because the automatic dilution of the smoke emissions in the box model results in lower rates of NO_x loss due to heterogeneous chemistry. In the 3-D model, the concentrated plume has high concentrations of NO_2 and aerosol particles, which results in a high rate of heterogeneous formation of HNO_3 and loss of NO_x. In the box model, the automatic dilution of the smoke emissions greatly reduces the concentrations of NO_2 and aerosol particles, and so the heterogeneous reaction rate for NO_2 is much slower.

[56] These results suggest that the GACM approach of automatic dilution can seriously overestimate the effective flux of NO_x to the global environment. This could lead to errors in model estimates of the global ozone formation from biomass burning emissions. It also shows that while the addition of heterogeneous reactions of NO_2 improves the match between model and observation for the Lagrangian and 3-D Eulerian plume models, simply adding this reaction to GACMs is unlikely to fix the NO_x overestimate, as the automatic dilution of the fire emissions would result in a slower rate of heterogeneous chemistry in GACMs.

4.2.3. Other NO_y Species

[57] Figure 21 shows the comparison between the box and 3-D models for the NO_y species: $HNO_{3(g)}$, aerosol nitrate (NO_3^-), total inorganic nitrate ($HNO_{3(g)}$ + NO_3^-), organic nitrate (AP1 through AP12 in ASP), PAN species (PAN1 through PN10 in ASP) and HONO. The total change in non-NH_3 nitrogen containing species (NO_x plus those listed above) is 10% higher in the box model runs than in the 3-D model. This error is consistent with that seen for other tracer species (like K^+), and is due to a combination of significant upward vertical diffusion of non-NH_3 nitrogen containing species, which have a high emission rate from the fire source but relatively low initial and background concentrations, and the condensation of organic nitrate species onto aerosols. This diffusive error helps to explain why estimates for many nitrogen containing species in the reference chemistry case are higher in the box model while the NO_x concentrations in the two models are very similar.

[58] For the reference chemistry case, the box model gives a much higher change in $HNO_{3(g)}$ ($\varepsilon_{HNO3(g)}$ = +164%) and a much lower change in aerosol nitrate than the 3-D model. In fact, the box model shows a reduction in aerosol nitrate with time, while the 3-D model shows a small increase. This is because the automatic dilution of emissions in the box model favors evaporation of semi-volatile species like nitrate to the gas phase, whereas modeling the concentrated plume results in a region of high $HNO_{3(g)}$ concentration in the smoke plume. Thus more of the total nitrate stays in the aerosol phase when the concentrated plume processes are modeled. The box model also gives a much higher change for total inorganic nitrate ($\varepsilon_{HNO_{3(g)}+NO_3^-}$ = +94%), total PAN (ε_{PAN} = +72%) and HONO (ε_{HONO} = +32%). These results are consistent with the higher ozone concentrations seen in the box model than in the 3-D model for the reference chemistry case, and are consistent with our previous conclusion that the box model approach results in a more oxidizing environment than in the 3-D model for the reference chemistry.

[59] For the expanded chemistry case, the box model gives a much lower change in inorganic nitrate than in the 3-D model ($\varepsilon_{HNO_{3(g)}+NO_3^-}$ = −52%). This is due to the much slower rate of heterogeneous HNO_3 formation when the plume emissions are automatically diluted in the box model versus the higher rate of heterogeneous reactions in the concentrated smoke plume. This underestimate of the rate of heterogeneous chemistry in the box model also explains the lower change in HONO seen in the box model (ε_{HONO} = −69%). The formation of organic nitrate is much higher in the expanded chemistry case than in the reference chemistry case because of the addition of BIOH. The concentrations of PAN predicted by the two models are fairly close (ε_{PAN} = −10%).

4.2.4. Aerosol Species

[60] Figure 22 shows the comparison between the box and 3-D models for aerosol chloride (Cl^-), aerosol sulfate (SO_4^{2-}), and aerosol organic carbon (OC). For both the reference and expanded chemistry cases, the total change in aerosol chloride is much lower in the box model (ε_{Cl-} = −84% and −72%, respectively) than in the 3-D model. This is consistent with the results for aerosol nitrate above, and is caused by the automatic dilution of fire emissions in the box model. In the concentrated smoke plume, high local concentrations of $HCl_{(g)}$ keep more of the total chloride in the aerosol phase. Automatically diluting the smoke emissions of chloride in the box model results in more of the chloride evaporating into the gas phase. As the 3-D model is already underestimating the amount of aerosol Cl^- relative to observations, the automatic dilution approach of GACMs may result in an even larger underestimate of aerosol Cl concentrations leaving biomass burning smoke plumes.

[61] For the reference chemistry case, the change in aerosol sulfate is larger in the box model than in the 3-D model ($\varepsilon_{SO_4^{2-}}$ = +24%), consistent with the results for O_3 and inorganic nitrate which both suggested that the box model approach results in a more oxidizing environment than in the 3-D model for the reference chemistry case. For the expanded chemistry case, the change in aerosol sulfate is smaller in the box model than in the 3-D model ($\varepsilon_{SO_4^{2-}}$ = −45%). This is consistent with the results for NO_x, total inorganic nitrate, and HONO, all of which suggest that the automatic dilution of smoke emissions in the box model leads to a much lower rate of heterogeneous chemistry in the box model than in the concentrated smoke plume.

[62] Aerosol organic carbon shows similar results to those for aerosol sulfate: the box model shows a smaller change than the 3-D model for the reference chemistry case and a larger change for the expanded chemistry case. However, the normalized differences between the box and 3-D models for OC (+13% and −9%) are of the same order as the differences due to vertical diffusion in the 3-D model, and so it is not clear if the differences due to nonlinear chemistry are significant for aerosol OC.

4.3. Effects of Shrinking and Expanding the Eulerian Box

[63] The above discussion leads to two additional questions. First, since the size of the Eulerian grid box evaluated so far (52.5 km × 20 km) is smaller than the general size of the grid boxes in GACMs, then how do the results change when the size of the box is increased? Second, does shrinking the box (for example, by reducing its scale in the cross-wind direction) reduce the differences between the box model and the 3-D plume model?

[64] To answer these questions, we ran two additional box model tests, one where we expanded the box to 100 km × 100 km in the horizontal, and one where we shrank the cross-wind extent of the box to 52.5 km × 10 km. Figure 23 compares the results of these tests with our previous box model and 3-D plume results for both the reference and expanded chemistry cases. For the reference chemistry case, shrinking the box generally provides a closer match to the 3-D plume model results. The results are more mixed for the expanded chemistry case, where shrinking the box makes the match worse for many species. For both chemistry cases, expanding the box to 100 km × 100 km dramatically increases the predicted formation of O_3, inorganic nitrate, and PAN and the destruction of NO_x relative to the 3-D plume model. The differences between the two chemistry cases for this large box are relatively small. Thus, the large boxes used in global models could substantially overestimate the effective emission of PAN and O_3 into the free troposphere from young smoke plumes, and mask the effects of heterogeneous chemistry within the smoke plumes.

5. Conclusions

[65] We have presented a 3-D Eulerian simulation of the fluid dynamics, gas-phase chemistry, aerosol chemistry, and the scattering and absorption of radiation within the Timbavati biomass burning smoke plume. To our knowledge, this is the first time all of these processes have been simulated simultaneously for a young biomass burning smoke plume. We considered two cases with different approaches to the chemistry. In the reference chemistry case, the uncharacterized organic species were assumed to be unreactive and heterogeneous chemistry was not included. In the expanded chemistry case, the uncharacterized compounds were included using BIOH (monoterpenes) as a proxy, and heterogeneous reactions of NO_2 and SO_2 were included with uptake coefficients of 10^{-3} and 2×10^{-4}, respectively.

[66] The 3-D Eulerian model does a good job matching the observed injection height of the smoke plume, but the initial model run underestimated the horizontal dispersion of the smoke plume. This underestimate may be due to an underestimate of subgrid-scale turbulent mixing or due to the fact that plume-scale fluctuations of the horizontal winds, which may be present in the convective boundary layer, are not simulated in the model. Increasing the minimum horizontal diffusion coefficient in the model provides a better match to the observed horizontal dispersion of the plume.

[67] The reference chemistry case underestimates the observed formation of O_3 while the expanded chemistry case provides a better match with observations. The maximum OH concentration predicted for the expanded chemistry case (1.0×10^7 radicals cm^{-3}) is still below the reported plume average OH concentration (1.7×10^7 radicals cm^{-3}), while the concentration of HONO for the expanded chemistry case is well below the detection limit for this species by AFTIR. Unfortunately this means that the accuracy of our HONO simulation cannot be assessed from these observations. The expanded chemistry case also gives lower NO_x concentrations than the reference case due to increased production of HNO_3.

[68] The model simulations suggest that direct measurements of OH in the young smoke plumes would be the best way to determine if heterogeneous production of HONO from NO_2 is taking place. An increase in OH while passing through the smoke plume would be consistent with the rapid heterogeneous formation of HONO from NO_2 on smoke particles, while a decrease in OH would suggest other explanations are required for the rapid formation of O_3 and nitrate in young biomass burning plumes. Thus, measurements of OH in young smoke plumes should be a priority for future field campaigns.

[69] The model matches well the observed downwind concentration of potassium, suggesting that the model is correctly reproducing the observed dispersion of the primary aerosol. However, the reference chemistry underestimates the observed secondary formation of OC, nitrate, and sulfate in the smoke plume, and underestimates the amount of chloride observed in the aerosol phase. The expanded chemistry case improves the match with observations, but still underestimates the observed aerosol concentrations. The maximum aerosol concentrations downwind are found at an altitude of 1 km, rather than the altitude of 0.6 km sampled in Timbavati. The total (gas + aerosol) amount of chloride downwind is consistent with the aerosol observations, but in the model the chloride is primarily in the gas phase. The concentration of total nitrate downwind is less than the observed aerosol nitrate concentration, suggesting that the model is underestimating the formation of nitrate from NO_x even in the expanded chemistry case. Simultaneous measurements of chloride and nitrate in the gas and aerosol phases would help to resolve these discrepancies by allowing us to close the budget for chloride and nitrogen atoms within the smoke plume.

[70] The modeled single scattering albedo for the aerosols in the expanded chemistry case is consistent with reported values for aged savannah smoke aerosols. The modeled aerosol scattering coefficient matches the observations fairly well for the first 10 km downwind from the fire, but underestimates the observed value further downwind. The comparison between modeled and observed aerosol number concentration is similar, with the model and observations agreeing fairly well from 0 to 10 km downwind of the source and then diverging. Thus, the underestimate in aerosol scattering coefficient downwind is likely related to the underestimate of aerosol number concentration downwind.

[71] Smoke aerosols reduce the modeled photolysis rates within and beneath the plume by 10–20%, and increased them above. However, the modeled solar heating due to the absorption of solar radiation is 4–6 K/d at 20–25 km downwind. This is somewhat lower than the reported value of 7.4 K/d, suggesting that the model may underestimate the absorption of solar radiation by the aerosols. This is consistent with the underestimate of BC relative to obser-

vations. Both discrepancies may be due to the absorption of solar radiation by secondary organic compounds, leading to an overestimate of BC in the observations and an underestimate of aerosol absorption in the model.

[72] We have evaluated the errors in the effective flux of gas and aerosol species to the global environment caused by the automatic dilution of biomass burning emissions into large-scale global model grid boxes. To accomplish this, we compared the results of our 3-D Eulerian plume simulation of the Timbavati smoke plume to the results of a single-box Eulerian model with the same horizontal scale (52.5 km $\times$ 20 km) as the full domain of our 3-D simulation. The Eulerian box model was run for both the reference and expanded chemistry cases.

[73] We found that the neglect of vertical diffusion of species into and out of the box model could result in errors of the order of $\pm(1-15)\%$ in the predicted total amounts of tracer species, depending on the initial concentration profile of the species, and hence the subsequent vertical gradients in the 3-D model when the fire emissions are included. Thus, changes of this order or less in other species may be caused by similar differences in advection and diffusion, by differences in nonlinear chemistry, or both. For the reference chemistry case, we found that the automatic dilution of emissions in the box model resulted in a more oxidizing environment, with a larger net formation of O_3 (+24%), total (gas plus aerosol) inorganic nitrate (+94%), PAN species (+72%), and aerosol sulfate (+24%). For the expanded chemistry case, the automatic dilution of emissions in the box model results in a lower heterogeneous reaction rate for NO_2 and SO_2. Thus, the automatic dilution of emissions leads to overestimates of NO_x (+40%), while total inorganic nitrate, HONO, and aerosol sulfate are underestimated (-52%, -69%, and -45%, respectively). The O_3 estimates for both models in the expanded chemistry case are very close (within 1%), while the PAN estimates are within 10% of each other. Aerosol organic carbon (OC) shows similar behavior to aerosol sulfate in both chemistry cases (+13% for reference chemistry, -9% for expanded chemistry), but the differences between the box and 3-D models are too small for us to rule out the possibility that they are caused by differences in advection and diffusion rather than the effect of dilution on the nonlinear chemistry. For both chemistry cases, the automatic dilution of emissions results in more of the total inorganic nitrate and chloride being present in the gas phase. Since the 3-D model is already underestimating the amount of aerosol nitrate and chloride downwind relative to emissions, this suggests that the GACM approach could result in substantial underestimates of these semivolatile aerosol constituents.

[74] This suggests that even if the chemical models for smoke plume chemistry are improved to better match the available observations, the automatic dilution of smoke plume emissions in GACMs could still result in large errors in predicted concentrations of O_3, NO_x and aerosol species downwind of biomass burning sources. These errors could change the predicted impact of biomass burning emissions on global chemistry and climate. For example, the overestimate of NO_x seen in the box model for the expanded chemistry case could result in an overestimate in the amount of global NO_x and O_3 formed by biomass burning emissions. It is also worth noting that even at the higher resolution of our 3-D smoke plume model, subgrid-scale processes are still present, and may lead to model errors in predicting the plume chemistry.

6. Potential Approaches for Global Atmospheric Chemistry Models

[75] There are several potential approaches to reduce the errors caused by the automatic dilution of plume emissions in GACMs. GACMs could use nested, higher-resolution grids over regions of intense biomass burning to allow them to better capture the nonlinear chemistry taking place in concentrated young smoke plumes. These nested grids could be static (fixed in space and time, as in the work by *Kumar and Russell* [1996]) or adaptive, where the grid system changes dynamically with time to meet solution requirements [*Srivastava et al.*, 2001]. One problem with this approach is that the required nested grid resolution may make the global model too computationally expensive to be of great use. Another issue is that the nested grid would have to be aligned along the motion of the plume, otherwise the cruder resolution at the boundaries would exacerbate the model errors. In addition, finer resolution models would eventually be limited by the resolution of the space-based data used to constrain the magnitude and variability of emissions.

[76] Another approach would be the use of a plume-in-grid model, where a subgrid-scale representation of the young smoke plumes is incorporated within the 3-D grid system of the GACM. Such plume-in-grid models have already been used to reduce the errors associated with the automatic dilution of smokestack emissions in urban and regional air quality models [e.g., *Karamchandani et al.*, 2002], and the work of *Freitas et al.* [2007] used an imbedded 1-D plume model to predict the effective plume height of biomass burning emissions for use in regional and global-scale models. A more detailed reactive plume model, incorporating a suitable gas- and aerosol-phase chemical model, could be used to estimate not only plume height, but the impact of plume chemistry on the effective emissions of biomass burning to the global environment. However, the few studies that have used this approach have used these models for case studies only, and this approach may also be too computationally expensive to implement.

[77] A third approach would be to develop a computationally efficient parametrization of the 3-D Eulerian plume model used in this work, and then to incorporate this parametrization into GACMs. This reduced form model could calculate the net export (effective emissions) of gas- and aerosol-phase species to the global environment from appropriate input parameters. This approach is currently used in the MIT Integrated Global Systems Model (IGSM) [*Prinn et al.*, 1999] to account for the impact of urban air chemistry on the effective emissions of several pollutants onto the global atmosphere. *Calbo et al.* [1998] developed a parametrization consisting of a set of analytical expressions to approximate the predictions of the California Institute of Technology–Carnegie-Mellon University (CIT) Urban Airshed Model [*McRae et al.*, 1982] for net export to the environment. *Mayer et al.* [2000] incorporated this parameterization into the MIT IGSM to study the impact of urban air pollution on global chemistry and climate. However, we

are not aware of any such parameterization available for smoke plume chemistry.

[78] No one modeling approach appears to be the ideal solution to the issues raised in this paper. However, all of these approaches would require accurate models of the gas- and aerosol-phase chemistry taking place in a young smoke plume, and would benefit from further research into these chemical models and smoke plume chemistry.

Appendix A: CRM6 Dynamics Model Equations

[79] This appendix describes the dynamical equations solved in the CRM6 3-D Eulerian dynamics model. All model equations are presented using Einstein's tensor notation.

A1. Continuity, Momentum, and Species Conservation Equations

[80] The CRM6 model divides all variables (F) into two parts: the grid-scale contribution ($\overline{F}$) and the subgrid-scale contribution (F'), so that

$$F = \overline{F} + F' \tag{A1}$$

In addition, the grid-scale variable $\overline{F}$ is divided into two parts: the value at a horizontally homogeneous hydrostatic state (F_0) and the deviation from this state (f)

$$\overline{F} = F_0 + f \tag{A2}$$

For notational convenience, $\overline{F}$ will be simplified to F in the equations below.

[81] The model framework is based on the pseudoelastic continuity equation of *Klemp and Wilhelmson* [1978]

$$\frac{\partial \pi}{\partial t} = \frac{c^2}{c_p \theta_{v0}^2 \rho_0} \frac{\partial \rho_0 \theta_{v0} u_j}{\partial x_j} \tag{A3}$$

where t is time, x_j is the spatial coordinate, u_j is the wind speed component along the j axis, c_p is the specific heat of air at constant pressure, ρ is the air density, θ_v is the virtual potential temperature. The quantity c^2 is given by the equation

$$c^2 = \left(\frac{c_p}{c_v}\right) R_d \theta_{v0} \Pi_o \tag{A4}$$

where c_v is the specific heat of air at constant volume, R_d is the gas constant for dry air, and Π is the nondimensional pressure, defined as

$$\Pi = \left(\frac{P}{P_o}\right)^{\frac{R_d}{c_p}} \tag{A5}$$

Note that

$$\pi = \Pi - \Pi_o \tag{A6}$$

and

$$\theta = \frac{T}{\Pi} \tag{A7}$$

[82] The momentum equations in flux form for the model are

$$\frac{\partial \rho u_i}{\partial t} + \frac{\partial \rho u_i u_j}{\partial x_j} = -\rho c_p \theta_{v0} \frac{\partial \pi}{\partial x_j} + \left[\frac{\theta}{\theta_0} - 1 + 0.61(q_v - q_{v0})\right] g \delta_{i3} + E_{u_i} \tag{A8}$$

where θ is the potential temperature, g is the acceleration due to gravity, and E_{ui} is the contribution by the subgrid-scale turbulent mixing of momentum.

[83] The thermodynamic equation is

$$\frac{\partial \rho \theta}{\partial t} + \frac{\partial \rho \theta u_j}{\partial x_j} = E_\theta + S_\theta \tag{A9}$$

where E_θ is the contribution of the subgrid-scale turbulent mixing of heat and S_θ is the fire source of sensible heat. Note that since we are not considering cloud particles here, the ice-liquid potential temperature used in CRM6 reduces to the potential temperature.

[84] The continuity equations for water vapor (q_v), trace gases (C_q), aerosol number (n_i), and aerosol mass concentrations ($c_{q,i}$) are all similar

$$\frac{\partial \rho q_v}{\partial t} + \frac{\partial \rho q_v u_j}{\partial x_j} = E_v + S_v \tag{A10}$$

$$\frac{\partial C_q}{\partial t} + \frac{\partial C_q u_j}{\partial x_j} = E_q + S_q \tag{A11}$$

$$\frac{\partial \rho n_i}{\partial t} + \frac{\partial \rho n_i u_j}{\partial x_j} = E_n + S_n \tag{A12}$$

$$\frac{\partial \rho c_{q,i}}{\partial t} + \frac{\partial \rho c_{q,i} u_j}{\partial x_j} = E_m + S_m \tag{A13}$$

with the E and S terms representing subgrid-scale turbulent mixing and the fire source, respectively.

A2. Subgrid-Scale Turbulent Mixing Parametrization

[85] The subgrid-scale mixing is parameterized using the first-order closure scheme of *Klassen and Clark* [1985]. For the unsaturated conditions studied here, the subgrid-scale terms in equations (A8) to (A13) are

$$E_{u_i} = \frac{\partial}{\partial x_j} K_M D_{ij} \tag{A14}$$

and

$$E_f = \frac{\partial}{\partial x_j} K_H \frac{\partial f}{\partial x_j} \tag{A15}$$

where f represents all scalar variables except u_i. D_{ij} is calculated from the flow as

$$D_{ij} = \frac{\partial u_i}{\partial x_j} + \frac{\partial u_j}{\partial x_i} - \frac{2}{3}\delta_{ij}\frac{\partial u_k}{\partial x_k} \quad (k = i = j \text{ when } i = j) \tag{A16}$$

and K_M is calculated as

$$K_M = \max\left[\frac{(0.15\Delta)^2}{\sqrt{2}}\left(\frac{1}{2}\sum_{i,j=1}^{3} D_{ij}^2\right) f(R_i), \frac{1}{3}K_{\min}\right] \quad \text{(A17)}$$

where

$$\Delta = \sqrt[3]{\Delta x \Delta y \Delta z} \quad \text{(A18)}$$

$$f(R_i) = \sqrt{1 - R_i} \quad (R_i < 1) \quad \text{(A19)}$$

$$= 0 \quad (R_i \geq 1) \quad \text{(A20)}$$

and R_i is the Richardson number calculated as

$$R_i = \frac{\frac{g}{\theta}\frac{\partial\theta}{\partial z}}{\left(\frac{\partial u_i}{\partial x_i}\right)^2} \quad \text{(A21)}$$

[86] Finally, $K_H = \max\,[3K_M, K_{\min}]$, where $K_{\min}$ is the user-assigned minimum value for the horizontal diffusivity of scalar tracers.

A3. Fire Source Terms

[87] The fire source terms are only nonzero at the surface of the model and in the horizontal boundaries of the fire source defined by $X_{fire} \leq x \leq X_{fire} + \Delta X_{fire}$; $Y_{fire} \leq y \leq Y_{fire} + \Delta Y_{fire}$, where ΔX_{fire} and ΔY_{fire} are the downwind and cross-wind dimensions of the fire source and X_{fire} and Y_{fire} are the coordinates of the corner of the fire source. Note that during the simulation X_{fire} moves with the fire front speed (0.5 m/s for Timbavati) while all other parameters of the fire source geometry remain constant.

[88] The source term for potential temperature S_θ (units of K s^{-1}) is derived form the sensible heat release rate of the fire Q_{heat} (units of W) as

$$S_\theta = \frac{Q_{heat}}{\rho c_p \Delta X_{fire} \Delta Y_{fire} \Delta z \Pi} \quad \text{(A22)}$$

[89] The source term for trace gases S_q (units of ppbm s^{-1}) are derived from the trace gas emission rate Q_q (kg s^{-1})

$$S_q = \frac{10^9 Q_q}{\rho \Delta X_{fire} \Delta Y_{fire} \Delta z} \quad \text{(A23)}$$

The values for Q_q are calculated using the emission rate of CO and the emission ratio of gas q to CO. Similarly, the source term for water vapor S_v (units of kg H_2O (kg air)$^{-1}$ s^{-1}) is

$$S_v = \frac{Q_v}{\rho \Delta X_{fire} \Delta Y_{fire} \Delta z} \quad \text{(A24)}$$

[90] The source terms for aerosol number and mass concentrations are calculated on the basis of the emission ratio of these species to CO

$$S_n = ER_{n_i/CO} S_{CO} \quad \text{(A25)}$$

$$S_m = ER_{c_{i,q}/CO} S_{CO} \quad \text{(A26)}$$

A4. Radiative Transfer and Photolysis Rates

[91] A δ-four-stream radiation module based on the model of *Fu and Liou* [1993] is included in the CRM6 model. We modified this module to include the radiative effects of aerosol particles interactively.

[92] The *Fu and Liou* [1993] module calculates the total upward and downward irradiances (in units of W m^{-2}) for 6 solar and 10 infrared radiation bands. However, as noted by *Madronich* [1987], the magnitudes of the irradiance and the actinic flux are not the same. The total actinic flux (F_{tot}) can be calculated from the downward direct, downward diffuse, and upward diffuse irradiances using the formula

$$F_{tot} = \frac{E_{direct}}{\cos\theta_z} + 2E_{\downarrow,diff} + 2E_{\uparrow,diff} \quad \text{(A27)}$$

[93] Since the radiation module of *Fu and Liou* [1993] does not separate the downward direct irradiance from the downward diffuse irradiance, we used the results of simulations with TUV v.4.1 to calculate the fraction of the downward irradiance due to the downward diffuse irradiance for 10 zenith angles between 0° and 86°. CRM6 then linearly interpolates those values to get the fraction of the downward flux due to the diffuse flux at the current zenith angle.

Appendix B: Eulerian Box Model Equations

[94] The continuity equations for the Eulerian box model, with widths ΔX and ΔY and height H are

$$\frac{dC_q}{dt} = \frac{q_q}{H} - \frac{v_{d,i}}{H} + \frac{U}{\Delta X}\left(C_q^o - C_q\right) + \left(\frac{dC_q}{dt}\right)_{cond} + \left(\frac{dC_q}{dt}\right)_{chem} \quad \text{(B1)}$$

$$\frac{dn_i}{dt} = \frac{q_i}{H} - \frac{v_{d,i}}{H} + \frac{U}{\Delta X}\left(n_i^o - n_i\right) + \left(\frac{dn_i}{dt}\right)_{cond} + \left(\frac{dn_i}{dt}\right)_{coag} \quad \text{(B2)}$$

$$\frac{dc_{q,i}}{dt} = \frac{q_{q,i}}{H} - \frac{v_{d,q,i}}{H} + \frac{U}{\Delta X}\left(c_{q,i}^o - c_{q,i}\right) + \left(\frac{dc_{q,i}}{dt}\right)_{cond} + \left(\frac{dc_{q,i}}{dt}\right)_{coag} + \left(\frac{dc_{q,i}}{dt}\right)_{chem} \quad \text{(B3)}$$

where C_q is the concentration of gas-phase species q (molecules/cm^3 air), n_i is the number concentration of particles in size bin i (particles/cm^3 air) and $c_{q,i}$ is the concentration of aerosol species q in size bin i (mol/cm^3 air). The first term on the right-hand side of each continuity equation represents the change in concentration due to emission of species from the fire source, with q_q representing the flux of species q from the fire source. We calculate q_q (mol/cm^2/s) from the species emission rate Q_q (mol/s) as $q_q = \frac{Q_q}{\Delta X \Delta Y}$.The second term represents the effect of deposition on the concentrations, where v_d is the deposition velocity. As in the Lagrangian studies of part 1 [*Alvarado and Prinn*, 2009], we set the deposition velocity equal to 0 for gas-phase species and use the terminal velocity of the aerosol particles as the deposition velocity for aerosol species. The third term represents the change due to horizontal winds transporting air into and out of the Eulerian box. Here C_q^o is the concentration of gas q in the

background air upwind of the fire site, U is the horizontal wind speed, and ΔX is the horizontal distance in the downwind direction. The remaining terms represent the change in gas- and particle-phase concentrations due to mass transfer between the gas and aerosol phases (*cond*), coagulation of particles (*coag*), and irreversible and reversible chemistry (*chem*). The calculation of these terms are performed by the ASP chemical model as described by *Alvarado* [2008] and *Alvarado and Prinn* [2009].

[95] **Acknowledgments.** This research was supported by an NSF Graduate Fellowship, a Martin Family Fellowship in Sustainability, an MIT Norman B. Leventhal Presidential Fellowship, NSF grant ATM-0120468, DOE grant DE-FG02-94ER61937, and the industrial and foundation sponsors of the MIT Joint Program on the Science and Policy of Global Change. We thank the reviewers for their helpful comments.

References

Alvarado, M. J. (2008), Formation of ozone and growth of aerosols in young smoke plumes from biomass burning, Ph.D. thesis, Mass. Inst. of Technol., Cambridge. (Available at http://mit.edu/cgcs/www/MIT_CGCS_Rpt78.pdf)

Alvarado, M. J., and R. G. Prinn (2009), Formation of ozone and growth of aerosols in young smoke plumes from biomass burning: 1. Lagrangian parcel studies, *J. Geophys. Res.*, doi:10.1029/2008JD011144, in press.

Andreae, M. O., and P. Merlet (2001), Emission of trace gases and aerosols from biomass burning, *Global Biogeochem. Cycles*, *15*(5), 955–966.

Barth, M., et al. (2007), Cloud-scale model intercomnparison of chemical constituent transport in deep convection, *Atmos. Phys. Chem.*, *7*, 4709–4731.

Calbo, J., W. Pan, M. Webster, R. G. Prinn, and G. J. McRae (1998), Parameterization of urban subgrid scale processes in global atmospheric chemistry models, *J. Geophys. Res.*, *103*(D3), 3437–3451.

Crutzen, P. J., and M. O. Andreae (1990), Biomass burning in the tropics: Impact on atmospheric chemistry and biogeochemical cycles, *Science*, *250*, 1669–1678.

Ekman, A. M. L., C. Wang, J. Ström, and R. Krejci (2006), Explicit simulation of aerosol physics in a cloud-resolving model: Aerosol transport and processing in the free troposphere, *J. Atmos. Sci.*, *63*, 682–696, doi:10.1175/JAS3645.1.

Ekman, A. M. L., A. Engström, and C. Wang (2007), The effect of aerosol composition and concentration on the development and anvil properties of a continental deep convective cloud, *Q. J. R. Meteorol. Soc.*, *133*, 1439–1452, doi:10.1002/qj.108.

Freitas, S., et al. (2007), Including the sub-grid scale plume rise of vegetation fires in low resolution atmospheric transport models, *Atmos. Chem. Phys.*, *7*, 3385–3398.

Fu, Q., and K. Liou (1993), Parameterizations of the radiative properties of cirrus clouds, *J. Atmos. Sci.*, *50*, 2008–2025.

Hobbs, P. V., P. Sinha, R. J. Yokelson, T. J. Christian, D. R. Blake, S. Gao, T. W. Kirchstetter, T. Novakov, and P. Pilewskie (2003), Evolution of gases and particles from a savanna fire in South Africa, *J. Geophys. Res.*, *108*(D13), 8485, doi:10.1029/2002JD002352.

Intergovernmental Panel on Climate Change (2001), *Climate Change 2001: The Scientific Basis*, Cambridge Univ. Press, Cambridge, U. K.

Jost, C., J. Trentmann, D. Sprung, M. O. Andreae, J. B. McQuaid, and H. Barjat (2003), Trace gas chemistry in a young biomass burning plume over Namibia: Observations and model simulations, *J. Geophys. Res.*, *108*(D13), 8482, doi:10.1029/2002JD002431.

Kaimal, J., J. Wyngaard, Y. Izumi, and O. Coté (1972), Spectral characteristics of surface layer turbulence, *Q. J. R. Meteorol. Soc.*, *98*, 563–589.

Karamchandani, P., C. Seigneur, K. Vijayaraghavan, and S.-Y. Wu (2002), Development and application of a state-of-the-science plume-in-grid model, *J. Geophys. Res.*, *107*(D19), 4403, doi:10.1029/2002JD002123.

Klassen, G., and T. Clark (1985), Dynamics of the cloud environment interface and entrainment in small cumuli: Two-dimensional simulation in the absense of ambient shear, *J. Atmos. Sci.*, *42*(23), 2621–2642.

Klemp, J. B., and R. B. Wilhelmson (1978), The simulation of three-dimensional convective storm dynamics, *J. Atmos. Sci.*, *35*, 1070–1096.

Kumar, N., and A. G. Russell (1996), Multiscale air quality modeling of the northeastern United States, *Atmos. Environ.*, *30*(7), 1099–1116.

Li, J., M. Posfai, P. V. Hobbs, and P. R. Buseck (2003), Individual aerosol particles from biomass burning in southern Africa: 2. Compositions and aging of inorganic particles, *J. Geophys. Res.*, *108*(D13), 8484, doi:10.1029/2002JD002310.

Lin, X., M. Trainer, and S. Liu (1988), On the nonlinearity of the tropospheric ozone production, *J. Geophys. Res.*, *93*(D12), 15,879–15,888.

Liousse, C., C. Devaux, F. Dulac, and H. Cachier (1995), Aging of savanna biomass burning aerosols: Consequences on their optical properties, *J. Atmos. Chem.*, *22*, 1–17.

Madronich, S. (1987), Photodissociation in the atmosphere: 1. Actinic flux and the effects of ground reflections and clouds, *J. Geophys. Res.*, *92*(D8), 9740–9752.

Mayer, M., C. Wang, M. Webster, and R. G. Prinn (2000), Linking local air pollution to global chemistry and climate, *J. Geophys. Res.*, *105*(D18), 22,869–22,896.

McRae, G., W. Goodin, and J. Seinfeld (1982), Development of a second generation mathematical model of urban air pollution—I. Model formulation, *Atmos. Environ.*, *16*, 679–696.

Posfai, M., R. Simonics, J. Li, P. V. Hobbs, and P. R. Buseck (2003), Individual aerosol particles from biomass burning in southern Africa: 1. Compositions and size distributions of carbonaceous particles, *J. Geophys. Res.*, *108*(D13), 8483, doi:10.1029/2002JD002291.

Prinn, R., et al. (1999), Integrated global system model for climate policy assessment: Feedbacks and sensitivity studies, *Clim. Change*, *41*(3–4), 469–546.

Pun, B. K.-L. (1998), Treatment of uncertainties in atmospheric chemical systems: A combined modeling and experimental approach, Ph.D. thesis, Mass. Inst. of Technol., Cambridge.

Reid, J. S., T. Eck, S. Christopher, R. Koppmann, O. Dubovik, D. Eleuterio, B. Holben, E. A. Reid, and J. Zhang (2005a), A review of biomass burning emissions part III: Intensive optical properties of biomass burning particles, *Atmos. Chem. Phys.*, *5*, 827–849.

Reid, J. S., R. Koppmann, T. Eck, and D. Eleuterio (2005b), A review of biomass burning emissions part II: Intensive physical properties of biomass burning particles, *Atmos. Chem. Phys.*, *5*, 799–825.

Seinfeld, J. H., and S. N. Pandis (1998), *Atmospheric Chemistry and Physics*, John Wiley, New York.

Srivastava, R., D. McRae, and M. Odman (2001), Simulation of dispersion of a power plant plume using an adaptive grid alogrithm, *Atmos. Environ.*, *35*, 4801–4818.

Stull, R. B. (1988), *An Introduction to Boundary Layer Meteorology*, Kluwer Acad., Dordrecht, Netherlands.

Trentmann, J., M. O. Andreae, H.-F. Graf, P. V. Hobbs, R. D. Ottmar, and T. Trautmann (2002), Simulation of a biomass-burning plume: Comparison of model results with observations, *J. Geophys. Res.*, *107*(D2), 4013, doi:10.1029/2001JD000410.

Trentmann, J., R. J. Yokelson, P. V. Hobbs, T. Winterrath, T. J. Christian, M. O. Andreae, and S. A. Mason (2005), An analysis of the chemical processes in the smoke plume from a savannah fire, *J. Geophys. Res.*, *110*, D12301, doi:10.1029/2004JD005628.

Trentmann, J., G. Luderer, T. Winterrath, M. Fromm, R. Servranckx, C. Textor, M. Herzog, H.-F. Graf, and M. Andreae (2006), Modeling of biomass smoke injection into the lower stratosphere by a large forest fire (part I): Reference simulation, *Atmos. Chem. Phys.*, *6*, 5247–5260.

Wang, C. (2005a), A modeling study of the response of tropical deep convection to the increase of cloud condensation nuclei concentration: 1. Dynamics and microphysics, *J. Geophys. Res.*, *110*, D21211, doi:10.1029/2004JD005720.

Wang, C. (2005b), A modeling study of the response of tropical deep convection to the increase of cloud condensation nuclei concentration: 2. Radiation and tropospheric chemistry, *J. Geophys. Res.*, *110*, D22204, doi:10.1029/2005JD005829.

Wang, C., and J. Chang (1993a), A three-dimensional numerical model of cloud dynamics, microphysics, and chemistry, *J. Geophys. Res.*, *98*, 14,827–14,844.

Wang, C., and J. S. Chang (1993b), A three-dimensional numerical model of cloud dynamics, microphysics, and chemistry: 2. A case study of the dynamics and microphysics of a severe local storm, *J. Geophys. Res.*, *98*, 14,845–14,862.

Wang, C., and R. G. Prinn (2000), On the roles of deep convective clouds in tropospheric chemistry, *J. Geophys. Res.*, *105*(D17), 22,269–22,297.

Yokelson, R. J., I. T. Bertschi, T. J. Christian, P. V. Hobbs, D. E. Ward, and W. M. Hao (2003), Trace gas measurements in nascent, aged, and cloud-processed smoke from African savanna fires by airborne fourier transform infrared spectroscopy (AFTIR), *J. Geophys. Res.*, *108*(D13), 8478, doi:10.1029/2002JD002322.

M. J. Alvarado, School of Engineering and Applied Science, Harvard University, 29 Oxford Street, Cambridge, MA 02138, USA. (mjalvara@seas.harvard.edu)

R. G. Prinn and C. Wang, Department of Earth, Atmospheric and Planetary Sciences, Massachusetts Institute of Technology, 77 Massachusetts Avenue, Building E19-467, Cambridge, MA 02139, USA. (rprinn@mit.edu; wangc@mit.edu)